JGR: Solid Earth

Supporting Information for

Reconciling the conflicting extent of overriding plate deformation before and during megathrust earthquakes in South America, Sunda Asia, and northeast Japan

Mario D'Acquisto[1], Taco Broerse[1], Celine P. Marsman[1], Rob Govers[1]

[1]Tectonophysics Group, Department of Earth Sciences, Utrecht University, Netherlands

Corresponding author: Mario D'Acquisto (m.dacquisto@uu.nl)

Contents of this file

Introduction

This supplementary material includes additional information on the processing steps used to process the published horizontal velocities from GNSS sites into interpolated fields of trench-perpendicular and trench-parallel velocities (Text S1, cf. Section 2 of the paper). We include an accompanying table of data sources for South America (Table S1) and Southeast Asia (Table S2). The figures are related to both the interpolation as well as the numerical modeling portion of the paper, and the latter show model results briefly discussed in Section 4. All modeling results, as described in Section 3, have been produced using the GTECTON finite element software package version *Parallel 2021.0.0* (Govers et al., 2018; Govers and Wortel, 2005, 1993).

Text S1: Estimating a backstop location from interseismic velocities

Collection of interseismic velocities

We collect estimates from horizontal velocities from published literature, for the South American margin, the Sunda margin and for (northern) Japan. The velocities are based on repeated GNSS campaign measurements or continuous GNSS observations, where the oldest measurements go back to the early 1990s, and the continuous observations are more recent.

We use velocities expressed in the global reference frame ITRF. A number of older studies expressed velocities for South America in a non-explicit stable South America reference frames, that likely differ between studies. Therefore, we use the tables from Kreemer et al. (2014), where a translation rate and rotation rate has been estimated for each published set of velocities, using overlapping sites from the various studies, to express velocities in the IGS08 reference frame (the IGS realization of ITRF). For these velocities, and those already expressed in the ITRF frame we apply the South America Euler pole of Kreemer et al. (2014). We also include velocities from Weiss et al. (2016), which are only provided in a self-determined, non-explicit South America reference frame; in that case, we show that the residuals between station velocities in that reference frame and velocities at the same stations from other studies (published in an ITRF and rotated into a South America frame) are extremely small.

Table S1 provides an overview of all data sources that we use for South America, including data periods and information on the reference system in which the velocities have been

provided by different studies. Table S2 contains the overview for Southeast Asia, where again we have made use of the data selection from Kreemer et al. (2014) that is expressed in a consistent reference frame. We add the GPS velocities for Java from Koulali et al. (2014) and apply their Euler pole to express the velocities in ITRF. Afterwards we apply the same Sunda Euler pole from Simons et al. (2007) to express velocities with respect to the overriding plate. As velocity estimates based on older campaign GNSS observations have higher uncertainties, the velocity field has a heterogeneous noise level. For Japan the velocities have also been taken from the collection of Kreemer et al. (2014), see table S3 for the original sources. We express the velocities for Japan in the Okhotsk frame from Kreemer et al. (2014).

As multiple earthquakes with magnitudes $M_w > 7.5$ have occurred along the South American, Sunda and Japan margins during the period of collecting GNSS data, coseismic offsets and postseismic transients potentially affect the velocity estimates. For this reason, we often have to resort to older studies that collected pre-earthquake data. We discard velocities from the database that have been derived from observations that may be affected by large earthquakes. As these earthquakes are thrust events, and thrusting leads mostly to coseismic and postseismic displacements towards the rupture, we assume that the affected areas are the areas located in the hinterland of the rupture. Furthermore, we do not consider data from sites in the vicinity of the 1960 Valdivia rupture, as postseismic relaxation due to the 1960 event has been ongoing (Wang et al., 2007). From the resulting dataset of inter-seismic velocities, we keep the velocity that has been estimated using the longest pre-earthquake time span of observations, as many sites have been revisited at later times.

Once we have obtained the two components of horizontal motion for each observation (Section 2 of the main text of the paper), we interpolate each component separately. First, we turn observations at locations less than 1 km apart into single data points by computing the weighted average of the geographical coordinates and the velocity components. In the averaging, we use the inverse of the observation variances as weights, i.e., the squares of the observation uncertainties. We rotate each individual horizontal velocity and associated

uncertainty to its local trench-perpendicular and trench-parallel direction (Figures S1-3), as described in main text section 2.2.

Interpolation: local ordinary kriging

We define a structured interpolation grid, with a spacing of 0.25 degrees (South America) or 0.1 degrees (Sunda and Japan) in longitude and latitude. We use all observations and their error variances at each interpolation grid point using ordinary kriging (Wackernagel, 2003), and apply kriging separately to the trench-perpendicular and trench-parallel velocities. Kriging uses correlograms to solve for interpolation weights. The mean, variance and correlation of the velocity components are strongly varying throughout the domain (i.e., the velocity field is only locally stationary). Therefore, we construct local correlograms in a similar manner as Fouedjio and Séguret (2016) and Machuca-Mory and Deutsch (2013). Correlograms describe the local variance of the observations and the correlation as a function of distance. We do not construct correlograms for each individual grid point, but define anchor points at every 3rd grid point (in both directions) for which we estimate a correlogram.

To incorporate local observations only in the experimental correlograms, we use a Gaussian kernel to apply a weight to the observed velocities, as a function of distance to the anchor point (Machuca-Mory and Deutsch, 2013). Next, we multiply the Gaussian kernel weight with the inverse of the observation variance to obtain neighbor weights for the local experimental correlograms.

The Gaussian kernel requires a length scale, and for this we introduce a natural neighborhood. First, we identify Voronoi cells, i.e., regions of space nearer to a single point than to other points. We determine the natural neighbors as the observation points whose Voronoi cells border the Voronoi cell of the anchor point (Sibson, 1981). These natural neighbors establish a natural neighborhood around each anchor point, and we define the natural neighborhood radius as the mean distance of the natural neighbors to the anchor. We define the Gaussian kernel width such that the kernel has a value of 0.5 at the natural neighborhood radius. To prevent that the observation variance is larger than the

correlogram variance (which leads to a discontinuous interpolated field), we require that the local variance is at least 4 times larger than the weighted average of the local observation variance. This we obtain by iteratively increasing the natural neighborhood radius until the requirement is met.

We fit an exponential correlogram (without nugget) to the local experimental correlogram using a Trust Region algorithm (Conn et al., 2000), where we apply the same Gaussian kernel to obtain fitting weights for each distance bin in the exponential correlogram. The range parameter determines the correlation length in the exponential correlogram, and we require the range to be at least 0.5 times the natural neighborhood radius (a smaller range may lead to absence of correlation between neigbouring observations and leads to discontinuities in the interpolated field).

We use natural neighbor interpolation (Sibson, 1981) to interpolate the correlograms from the anchor points to all points on the finer interpolation grid. Next, we apply ordinary kriging with the interpolated local correlograms at each individual grid point to obtain an interpolated velocity and associated uncertainty. Figures 2-4 show the resulting interpolated velocity fields, and Figures S10-12 depict the associated velocity uncertainties. The kernel widths and correlogram parameters used in the kriging are shown in Figures S4–S9. In the main text, Figures 2-4 show the interpolated velocity field, the associated uncertainties can be found in Figures S10-S12.

Hurdle estimation

We estimate hurdle distances along trench-perpendicular profiles, using the trench-perpendicular and trench-parallel velocity field and associated uncertainties. To do so, we resample the velocity fields and uncertainties using bilinear interpolation. We show a selection of these cross-sections in Figures 2-4. We express the velocities and uncertainties as function of distance along a profile. To estimate a hurdle location we fit a function f consisting of two linear segments to the velocity y_i where the breakpoint α between the two lines describes the hurdle distance:

$$y_i = f(x_i, \theta, \alpha) + \epsilon_i$$

with the continuous two segment function *f* as a function distance x_i *a*nd bias and slope parameters θ

$$f(x_i, \theta, \alpha) = \begin{cases} \theta_1 + \theta_2 x_i, & x_i \leq \alpha \\ \theta_3(x_i - \alpha) + \theta_1 + \theta_2 x_i, & x_i > \alpha \end{cases}$$

Using weighted non-linear least squares we minimize the following, using a Trust Region algorithm, applying the standard deviations σ_i estimated in the local kriging as weights.

$$\min\left(\boldsymbol{\Sigma_{i=1}^{n}}\left(\frac{\boldsymbol{f(x_i, \theta, \alpha) - y_i}}{\boldsymbol{\sigma_i}}\right)^{\mathbf{2}}\right)$$

To estimate uncertainties of the parameters (including the hurdle distance), we linearize at the parameter estimates $\hat{\theta}$, $\hat{\alpha}$ such that we can propagate the velocity uncertainties to obtain the variances of the estimated parameters.

$$\mathbf{C_{\hat{\theta},\hat{\alpha}} = \left(J^T C_y^{-1} J\right)^{-1}}$$

Here the inverse covariance matrix C_y^{-1} of the velocity fields is a diagonal matrix:

$$C_y^{-1} = \mathrm{diag}\left(\frac{1}{\sigma^2}\right)$$

And J is the Jacobian matrix, describing the dependence of the function *f* to variation in the estimated parameters:

$$J = \frac{\partial f\left(x, \hat{\theta}, \hat{\alpha}\right)}{\partial \theta, \alpha}$$

Numerically evaluated at the estimate for θ and α.

We compute the 95% confidence bounds of the hurdle distance by:

$$\hat{\alpha} \pm t(0.025, n - p)\sigma_{\hat{\alpha}}$$

using the Student's t-distribution, using n observations and p estimated parameters.

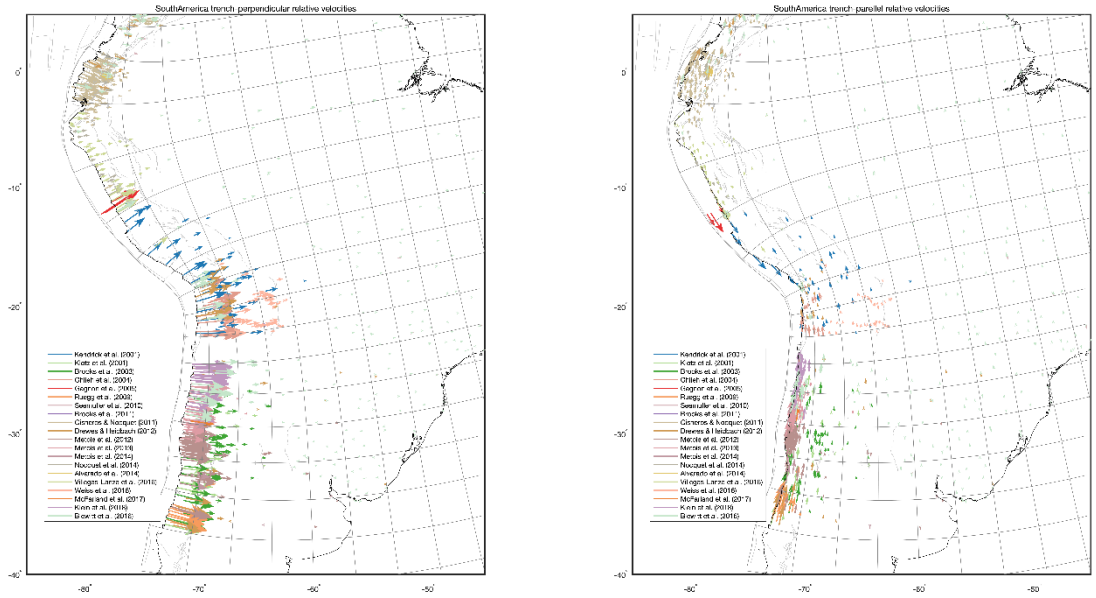

Figure S1 Decomposition of interseismic velocities in the South America plate reference into trench-perpendicular and trench-parallel velocities.

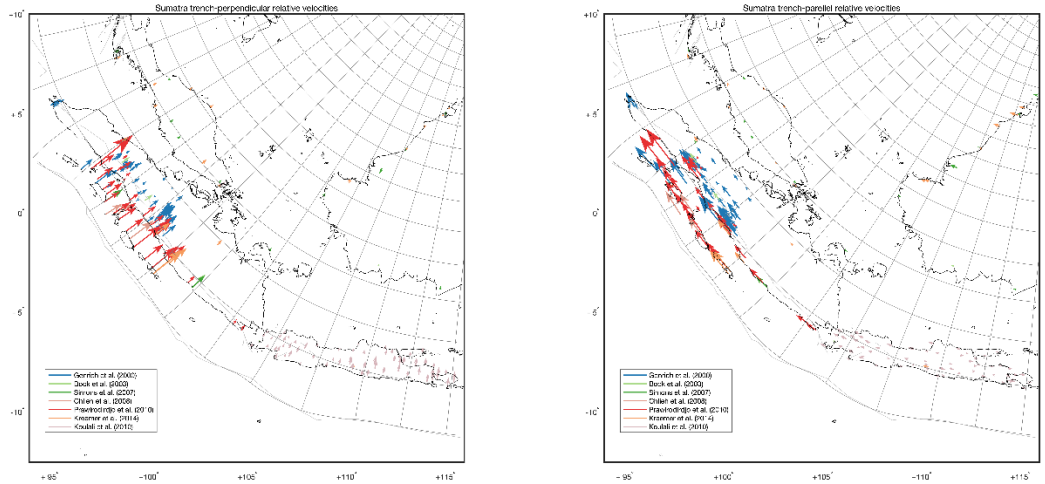

Figure S2 Decomposition of interseismic velocities in the Sunda plate reference into trench-perpendicular and trench-parallel velocities.

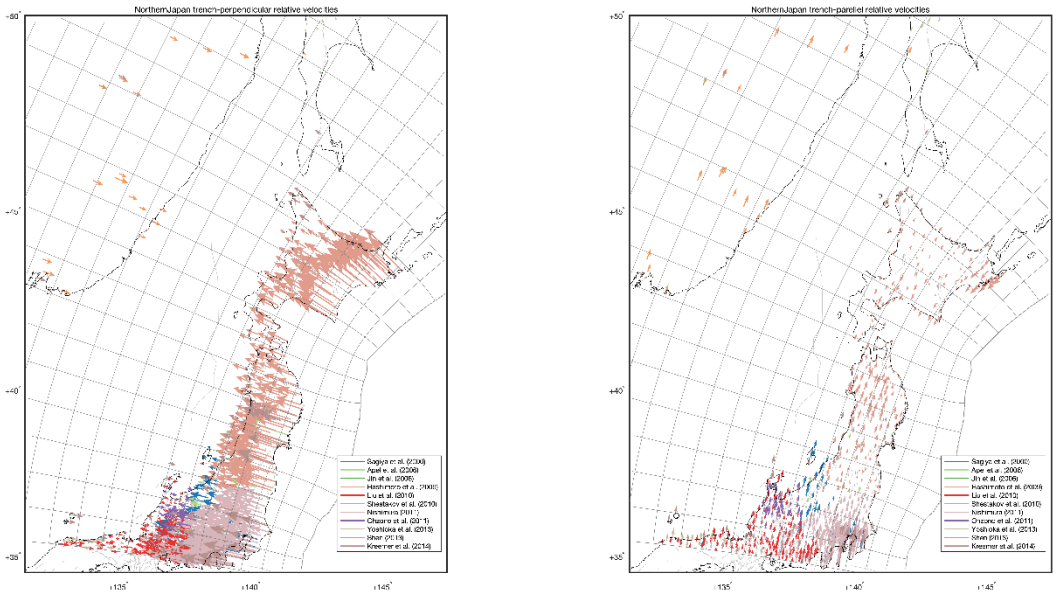

Figure S3 Decomposition of Honshu and Hokkaido interseismic velocities in the Okhotsk plate reference into trench-perpendicular and trench-parallel velocities.

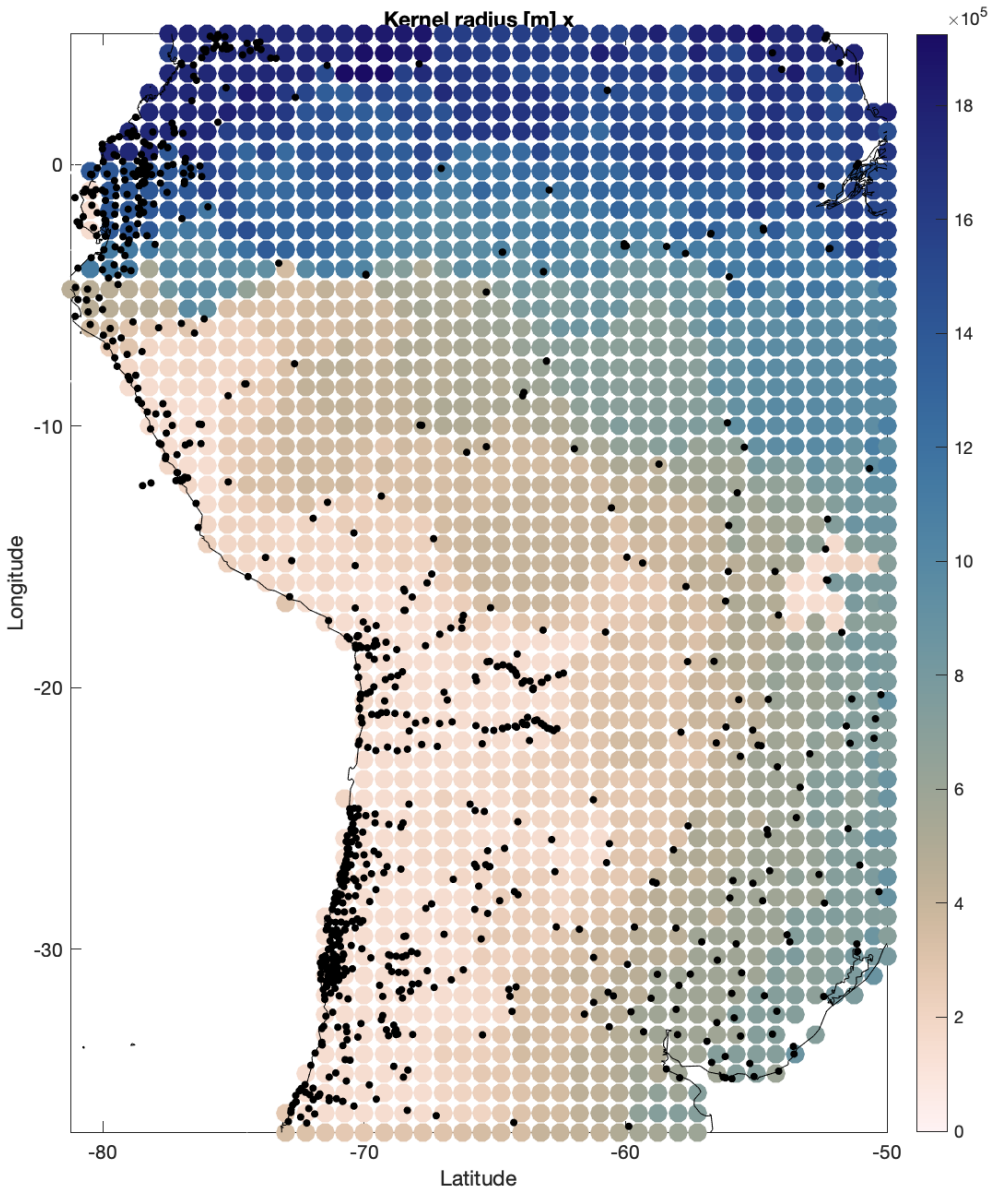
Kernel radius [m] x
×10^5
18
16
14
12
10
8
6
4
2
0
0
-10
-20
-30
Longitude
-80
-70
-60
-50
Latitude

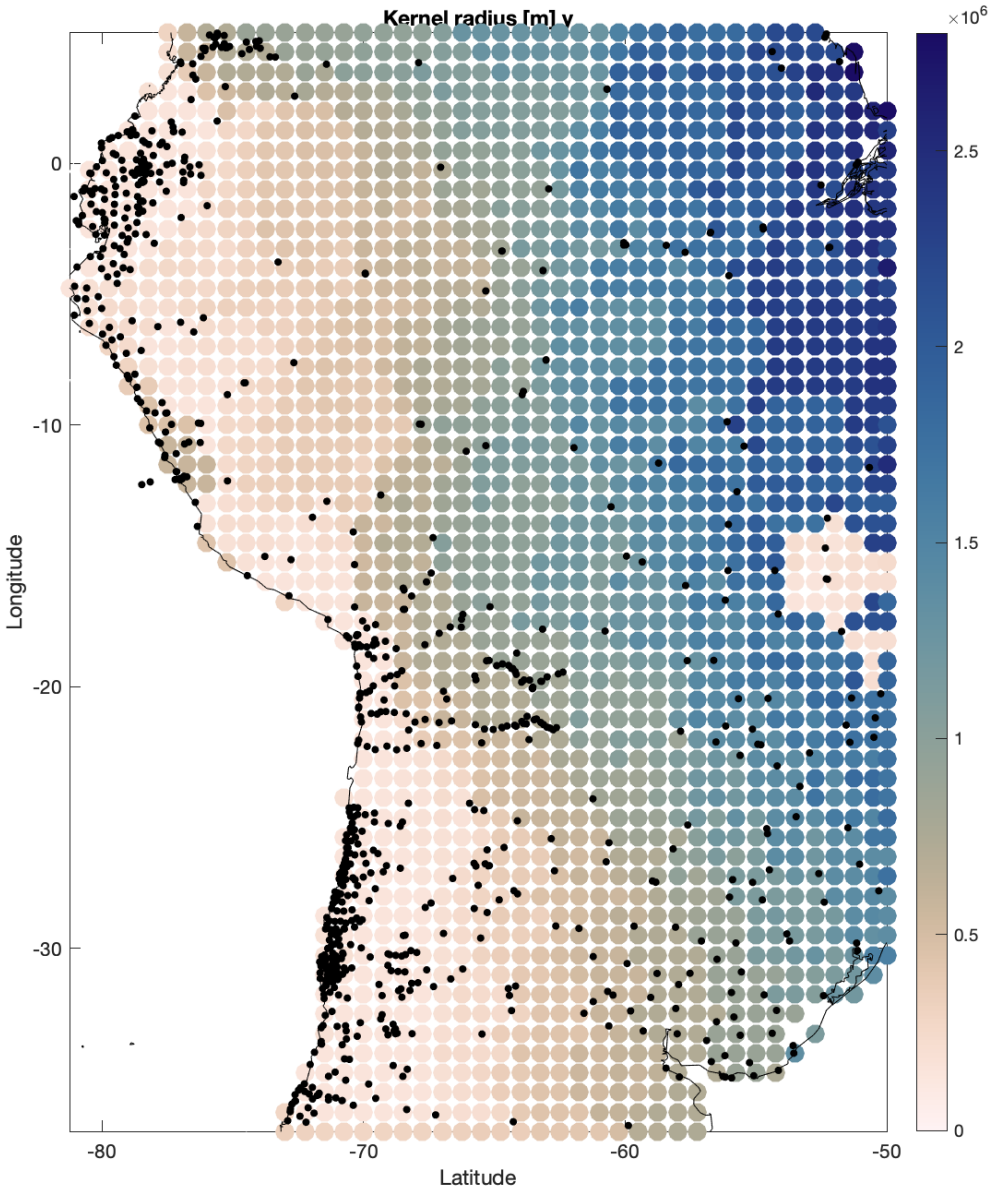

Figure S4 Gaussian kernel radius for the weighting of trench-perpendicular (x) and trench-parllel (y) velocities in constructing the local corellogram at each anchor point in South America. Black dots denote GNSS observation points. As the kernel is defined based on the distance to natural neighbors of the anchor point, densely sampled areas (often near-trench) have a narrow weighting kernel, while sparsely sampled areas have a wide weighting kernel. In some areas a low signal-to-noise may lead to a kernel radius that is larger than the natural neighborhood, to prevent relatively large nugget values, compared to the correlogram variance.

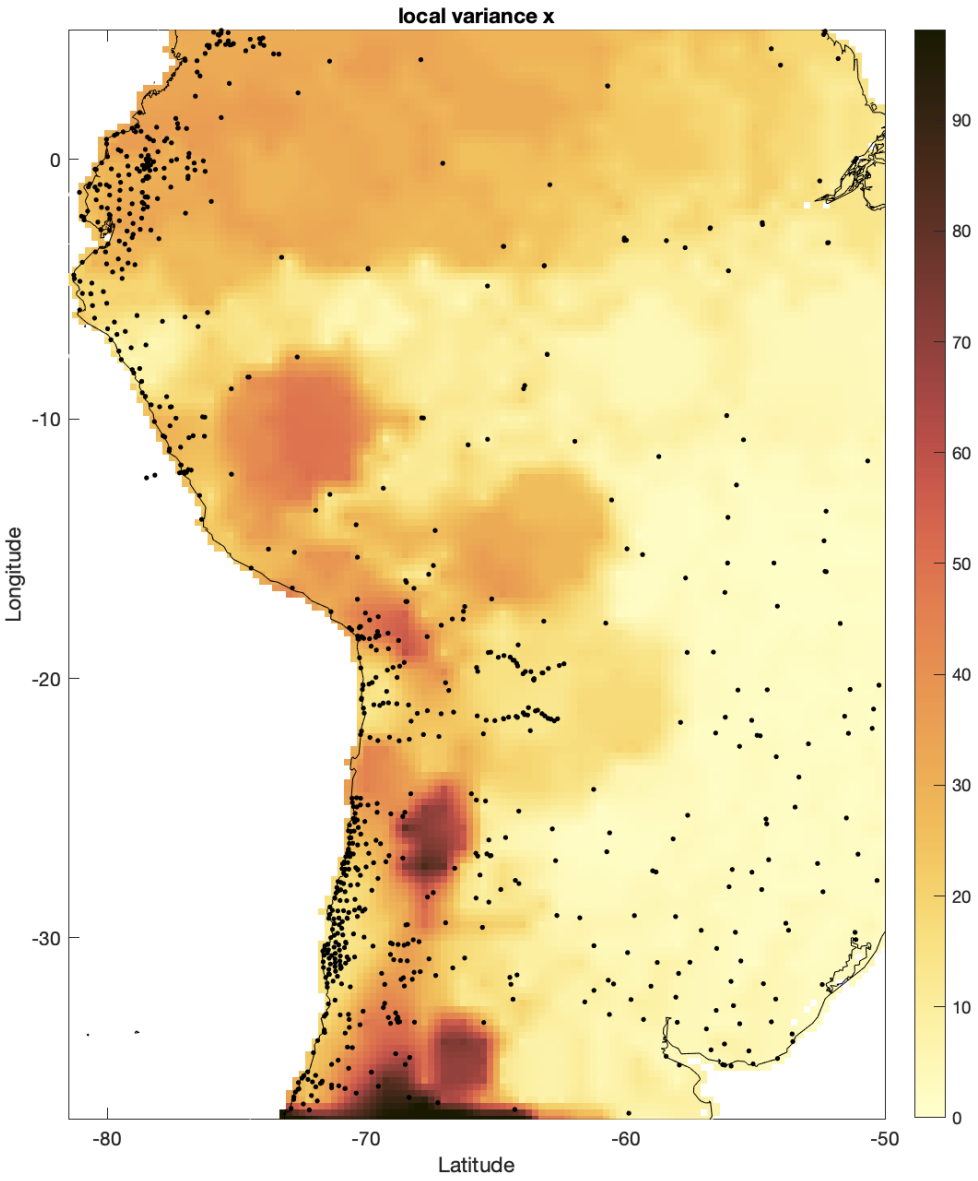
local variance x
0
-10
-20
-30
Longitude
-80
-70
-60
-50
Latitude
90
80
70
60
50
40
30
20
10
0

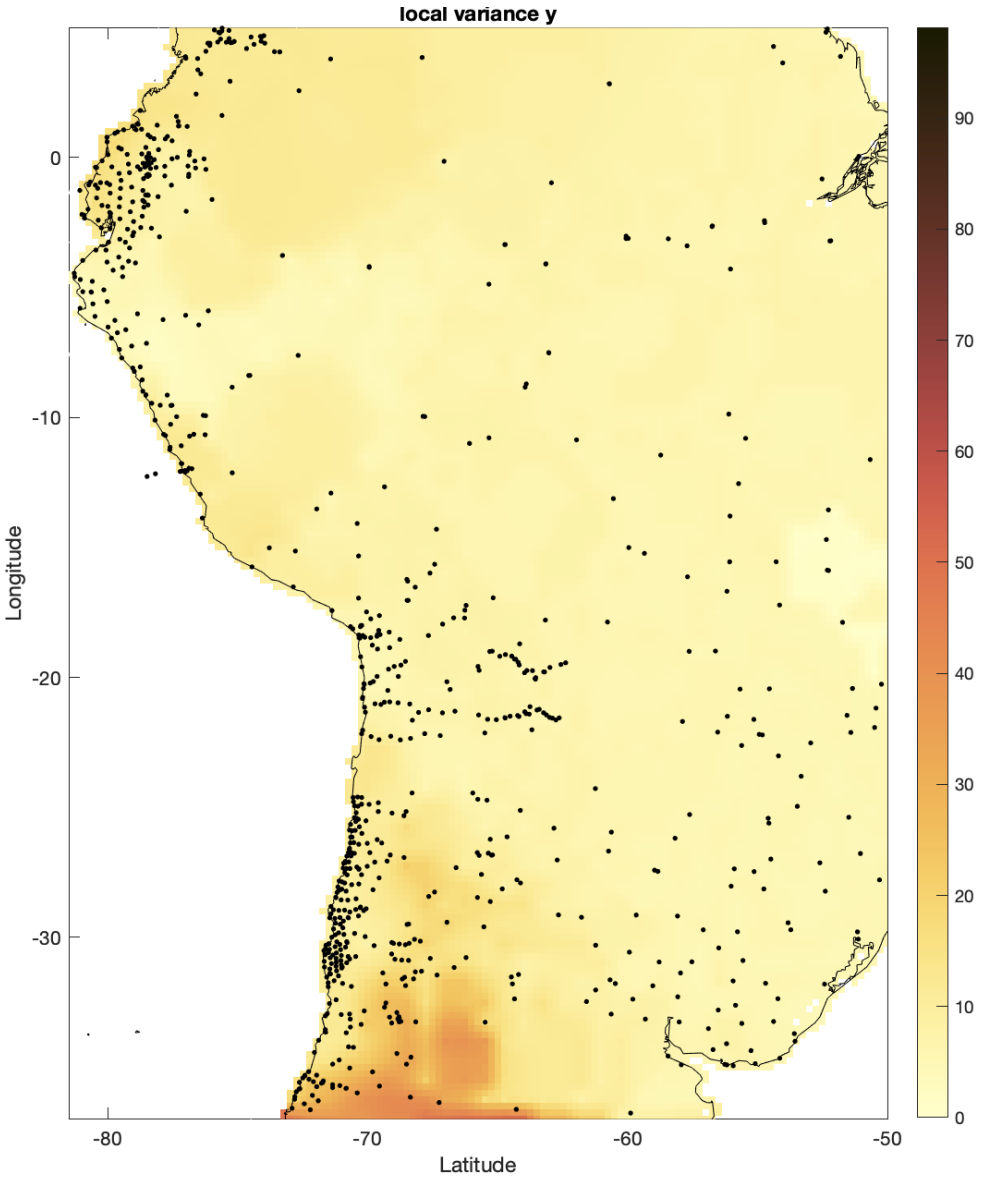
local variance y
0
-10
-20
-30
Longitude
-80
-70
-60
-50
Latitude
90
80
70
60
50
40
30
20
10
0

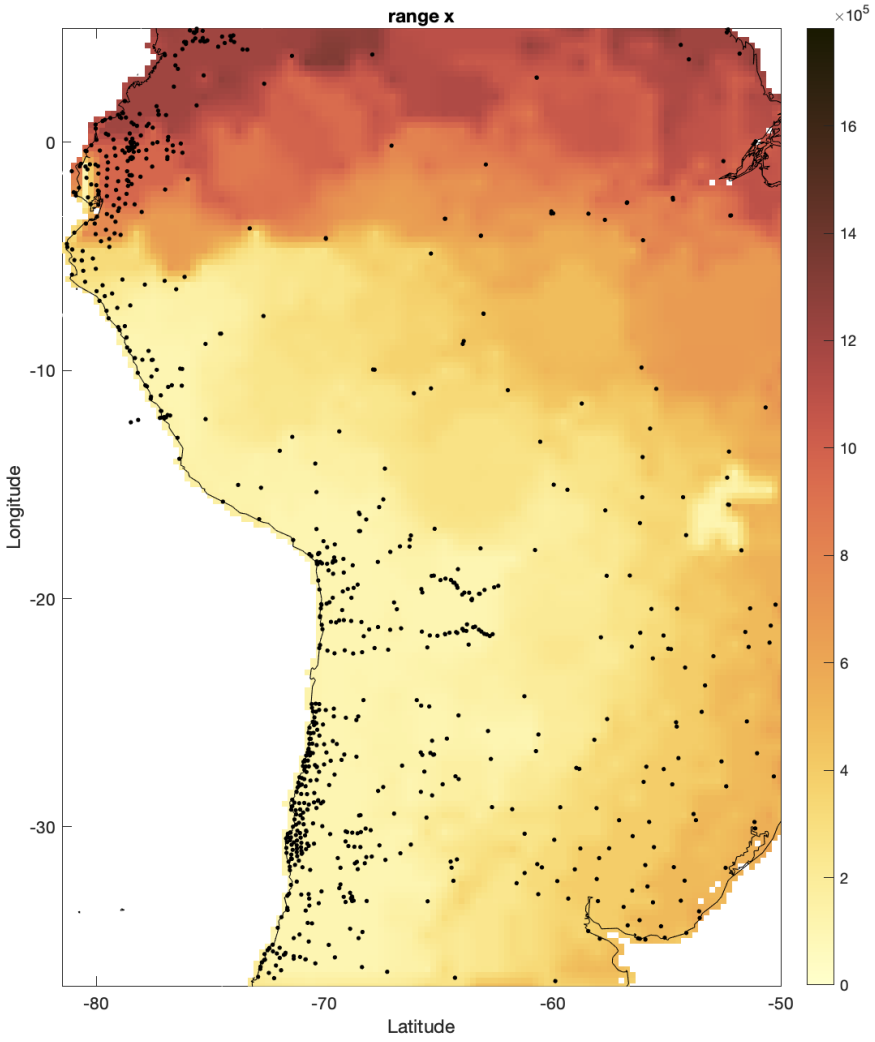
range x
×10^5
16
14
12
10
8
6
4
2
0
0
-10
-20
-30
Longitude
-80
-70
-60
-50
Latitude

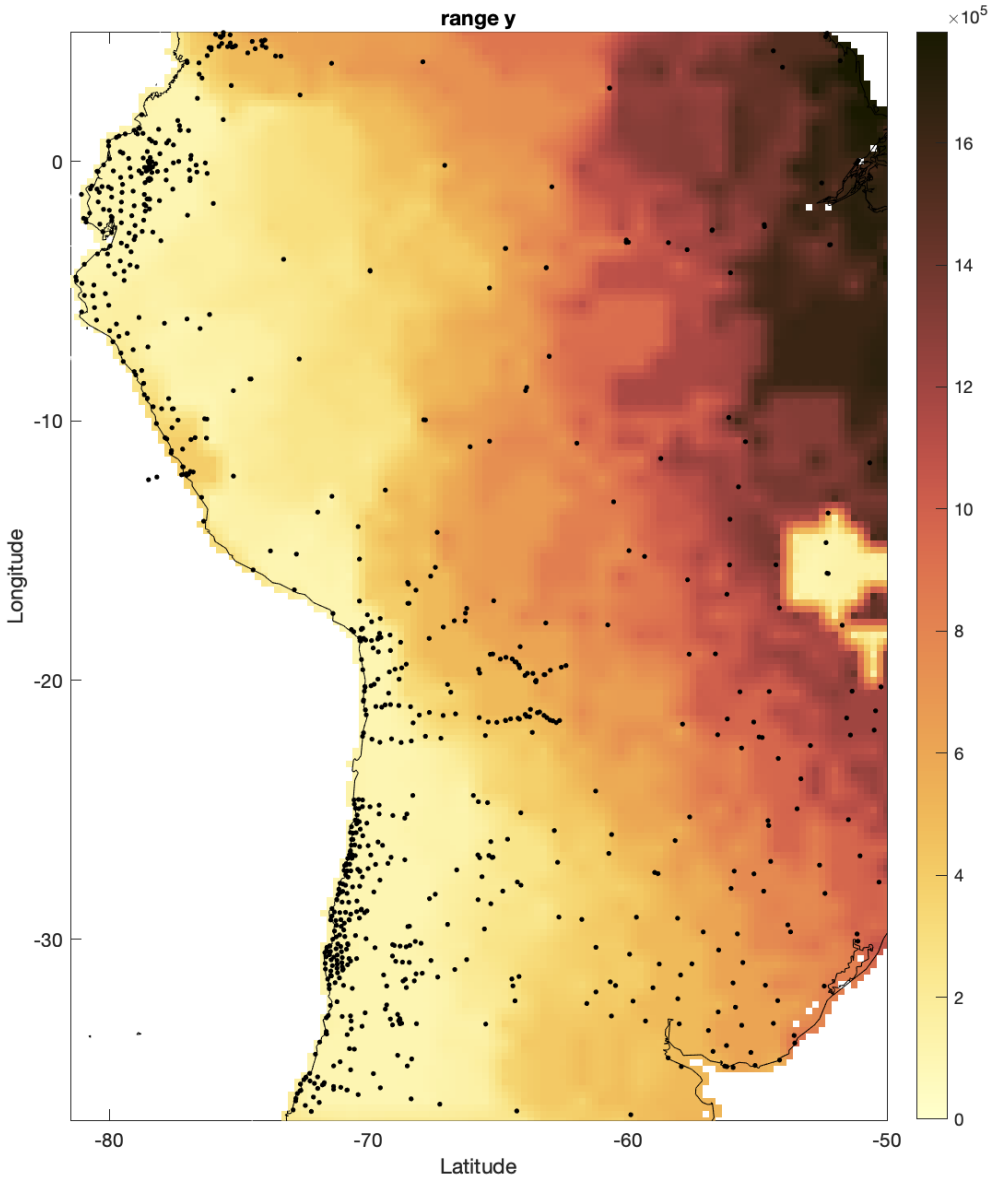

Figure S5 Estimated local correlogram (exponentional) parameters: range and variance, for trench-perpendicular (x) and trench-parallel (y) velocities in South America. Range (in meters) describes the decay of the correlation with distance, variance denotes the local observation variance (in mm^2/yr^2). The variance is generally larger if the observation changes much within a natural neighborhood (roughly in between observation points) or in some cases, when the kernel radius is large because of a low signal-to-noise.

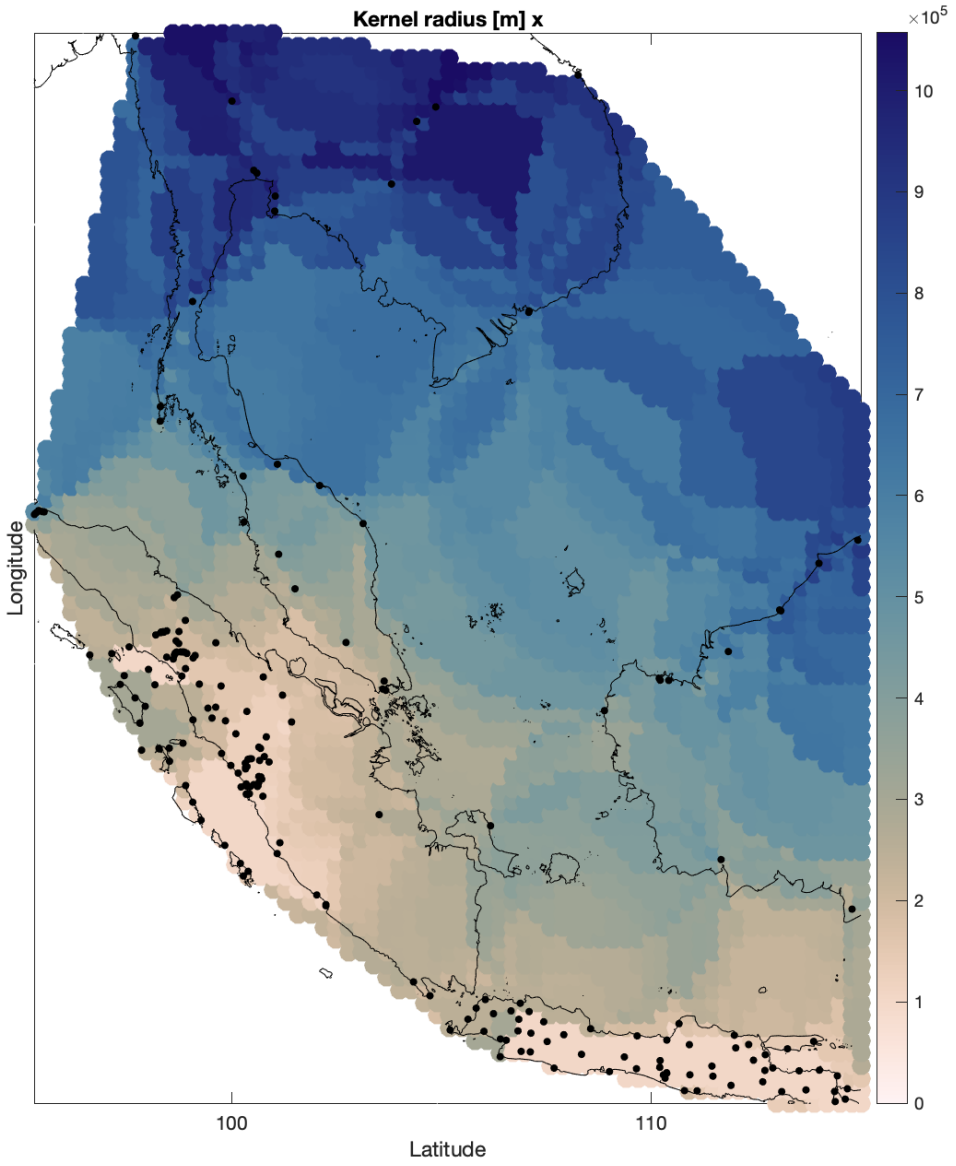
Kernel radius [m] x
×10^5
10
9
8
7
6
5
4
3
2
1
0
Longitude
100
110
Latitude

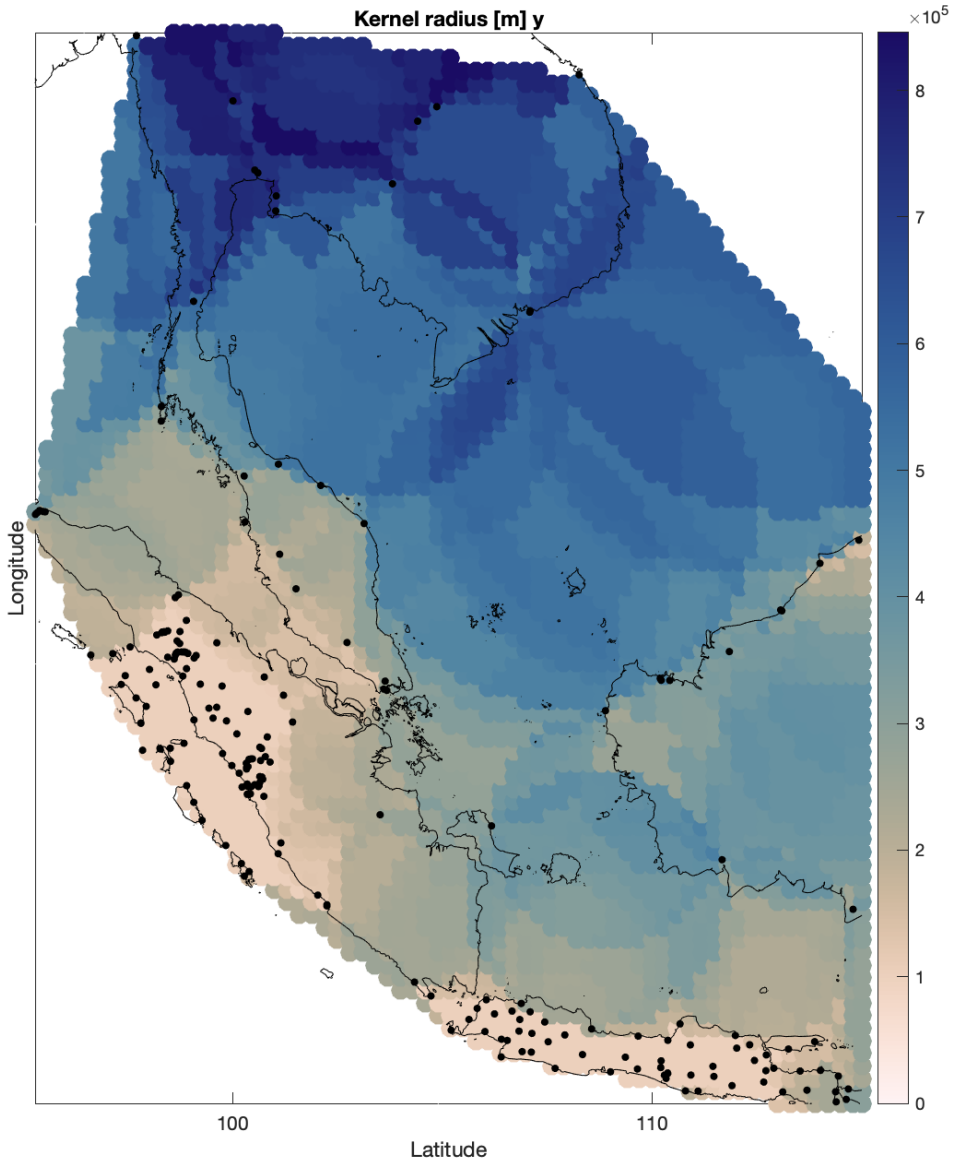

Figure S6 Gaussian kernel radius for the weighting of trench-perpendicular (x) and trench-parallel (y) velocities in constructing the local corellogram at each anchor point in Southeast Asia. Black dots denote GNSS observation points. As the kernel is defined based on the distance to natural neighbors of the anchor point, densely sampled areas (often near-trench) have a narrow weighting kernel, while sparsely sampled areas have a wide weighting kernel. In some areas a low signal-to-noise may lead to a kernel radius that is larger than the natural neighborhood, to prevent relatively large nugget values, compared to the correlogram variance.

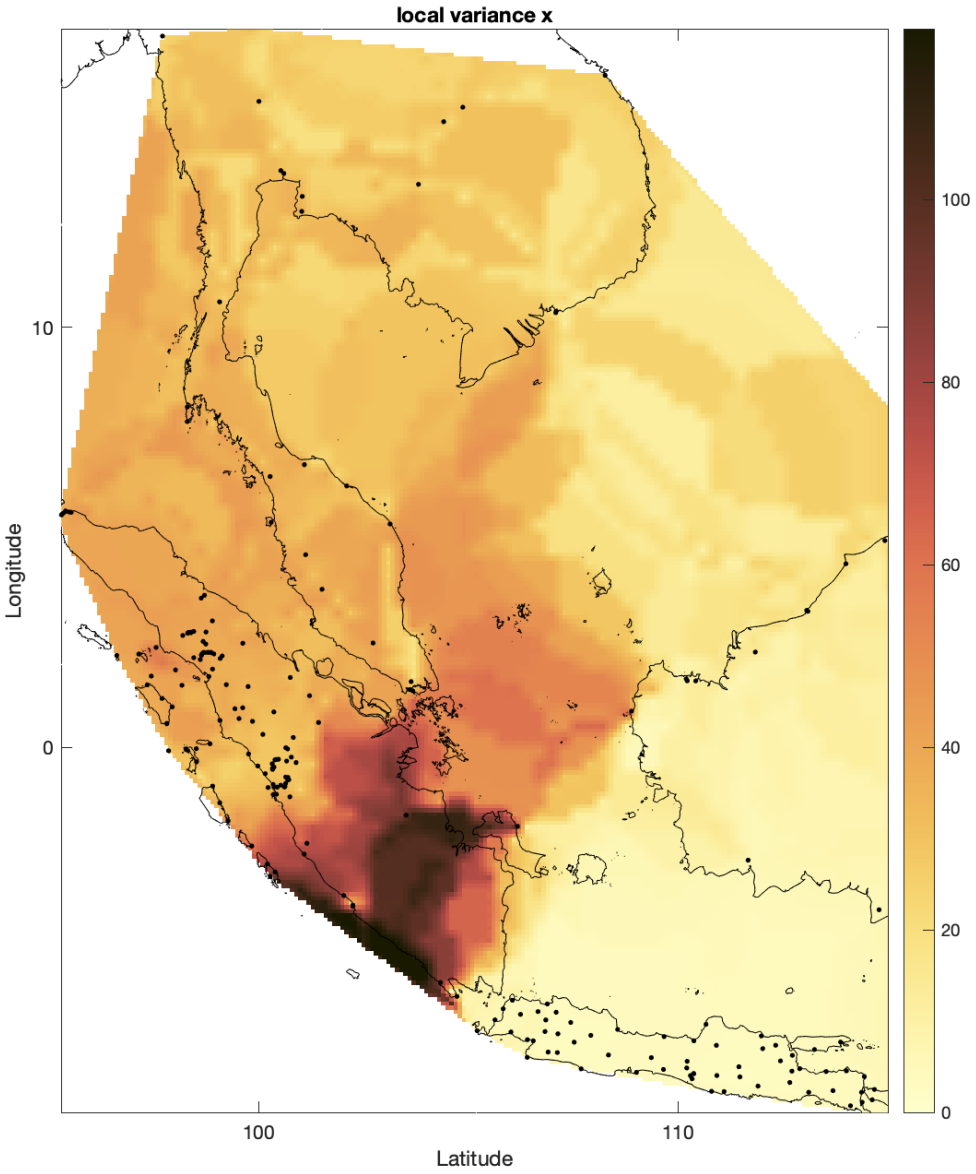
local variance x
Longitude
10
0
100
110
Latitude
100
80
60
40
20
0

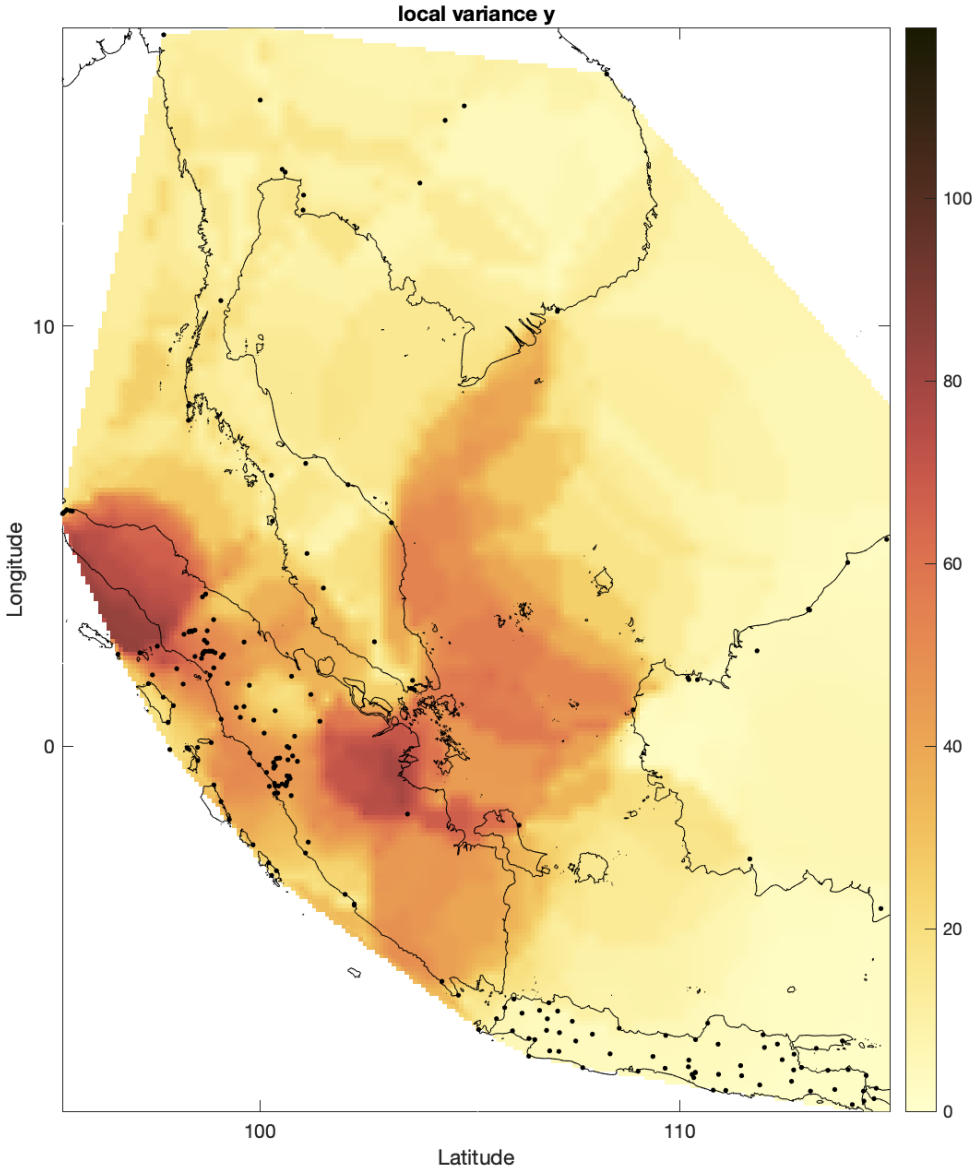
local variance y
Longitude
10
0
100
110
Latitude
100
80
60
40
20
0

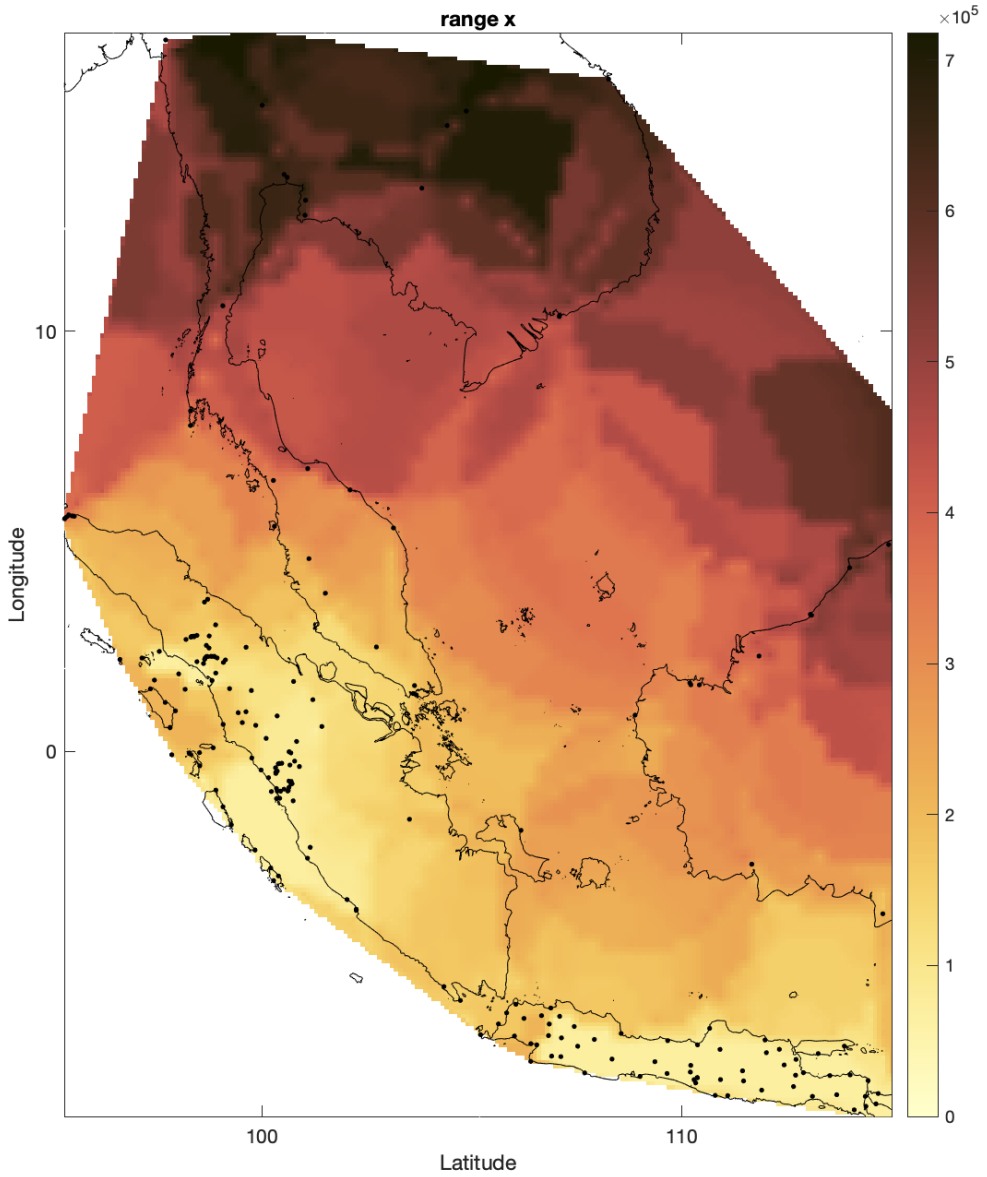
range x
×10^5
7
6
5
4
3
2
1
0
10
0
Longitude
100
110
Latitude

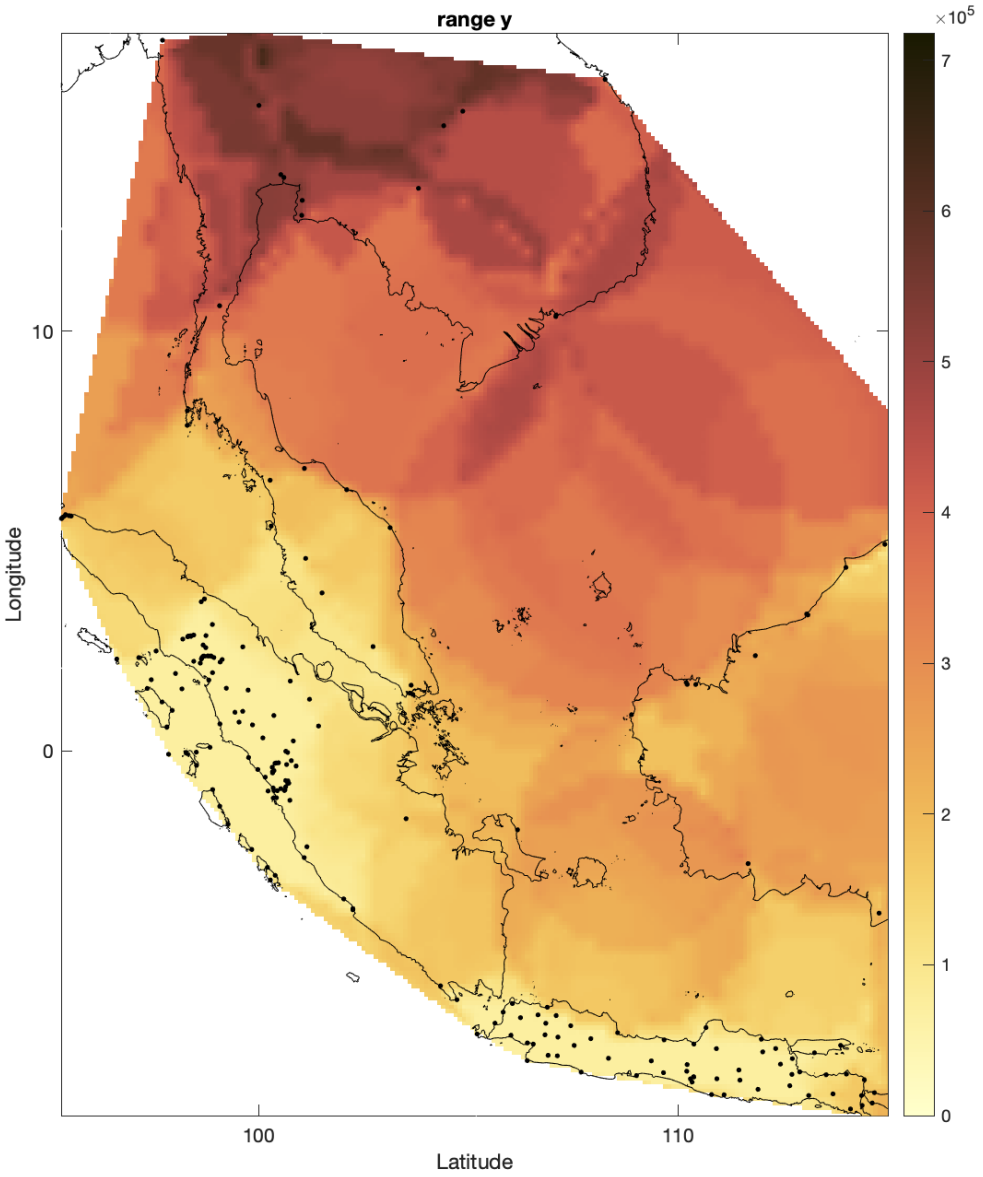

Figure S7 Estimated local correlogram (exponentional) parameters: range and variance, for trench-perpendicular (x) and trench-parallel (y) velocities in Southeast Asia. Range (in meters) describes the decay of the correlation with distance, variance denotes the local observation variance (in mm^2/yr^2). The variance is generally larger if the observation changes much within a natural neighborhood (roughly in between observation points) or in some cases, when the kernel radius is large because of a low signal-to-noise.

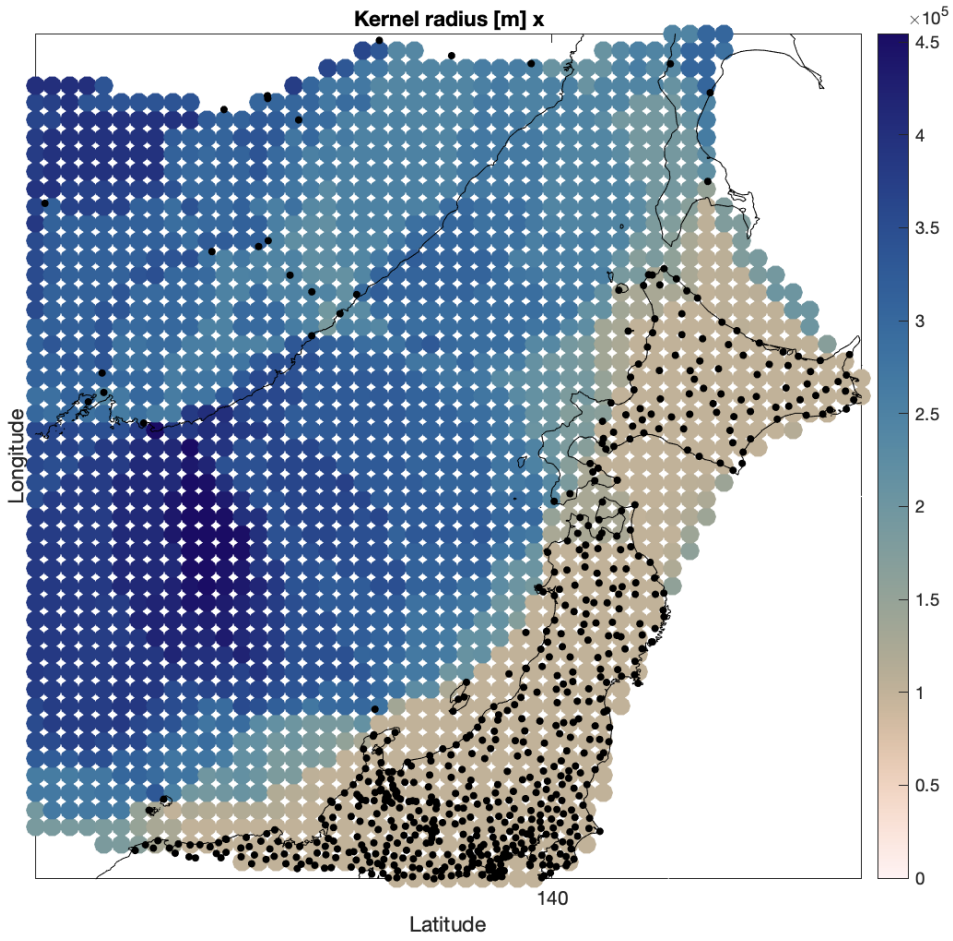
Kernel radius [m] x
×10^5
4.5
4
3.5
3
2.5
2
1.5
1
0.5
0
Longitude
140
Latitude

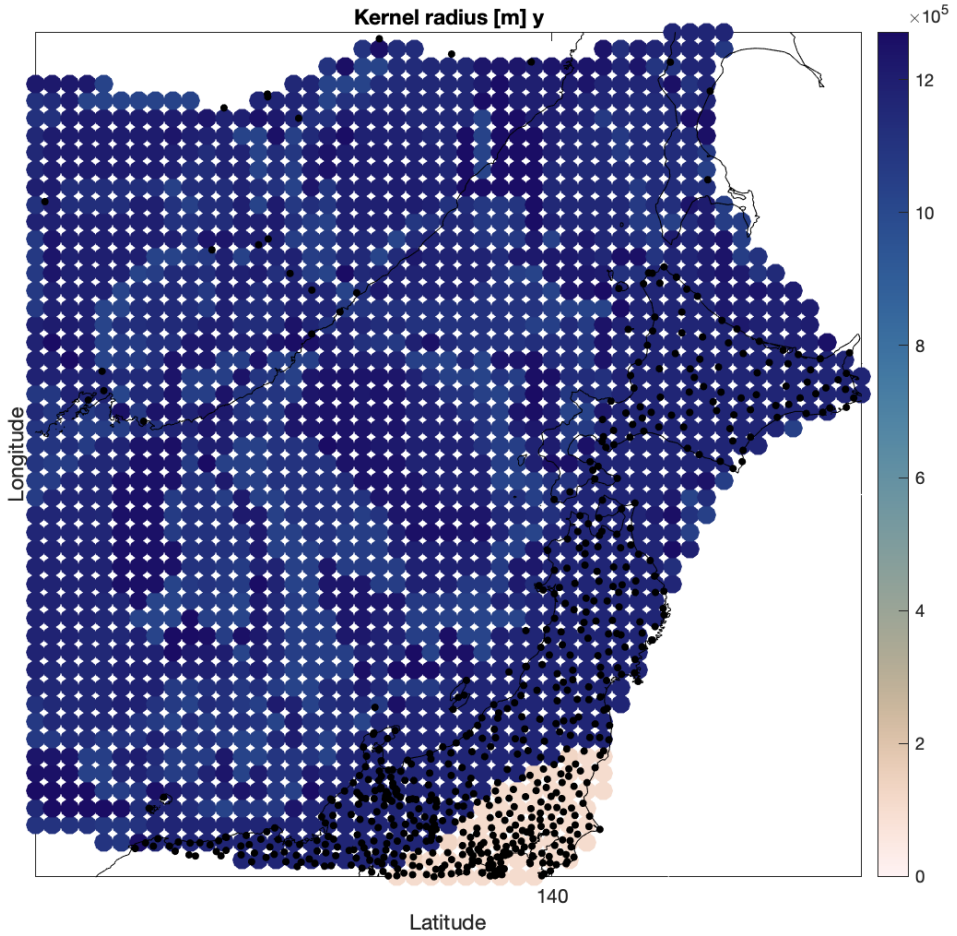

Figure S8 Gaussian kernel radius for the weighing of trench-perpendicular (x) and trench-parallel (y) velocities in constructing the local corellogram at each anchor point in Japan. Black dots denote GNSS observation points. As the kernel is defined based on the distance to natural neighbors of the anchor point, densely sampled areas (often near-trench) have a narrow weighting kernel, while sparsely sampled areas have a wide weighting kernel.

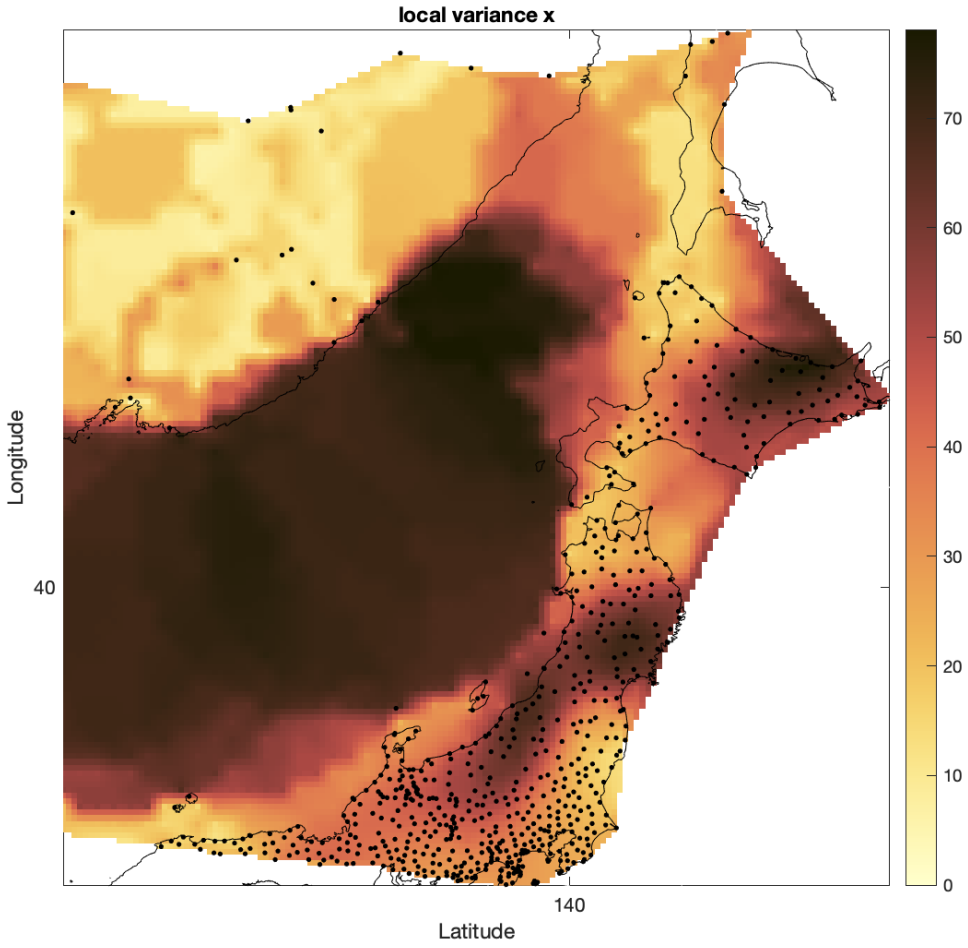
local variance x
Longitude
40
140
Latitude
70
60
50
40
30
20
10
0

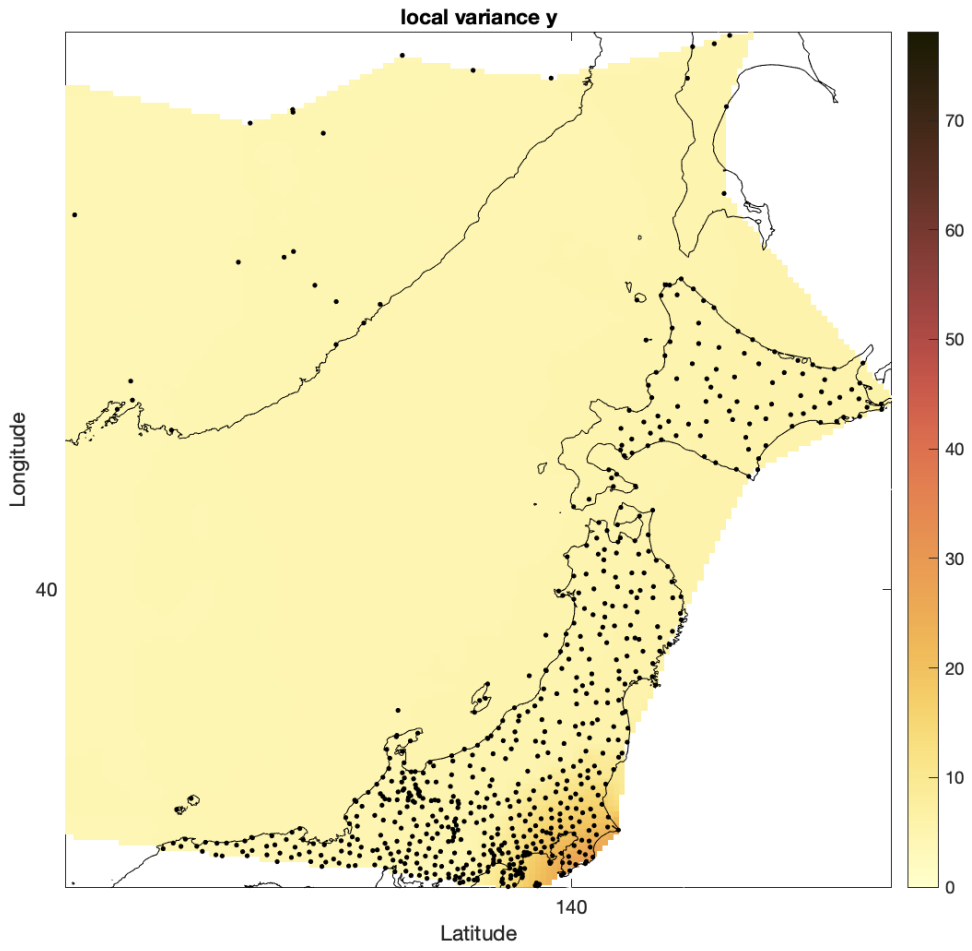
local variance y
Longitude
40
140
Latitude
70
60
50
40
30
20
10
0

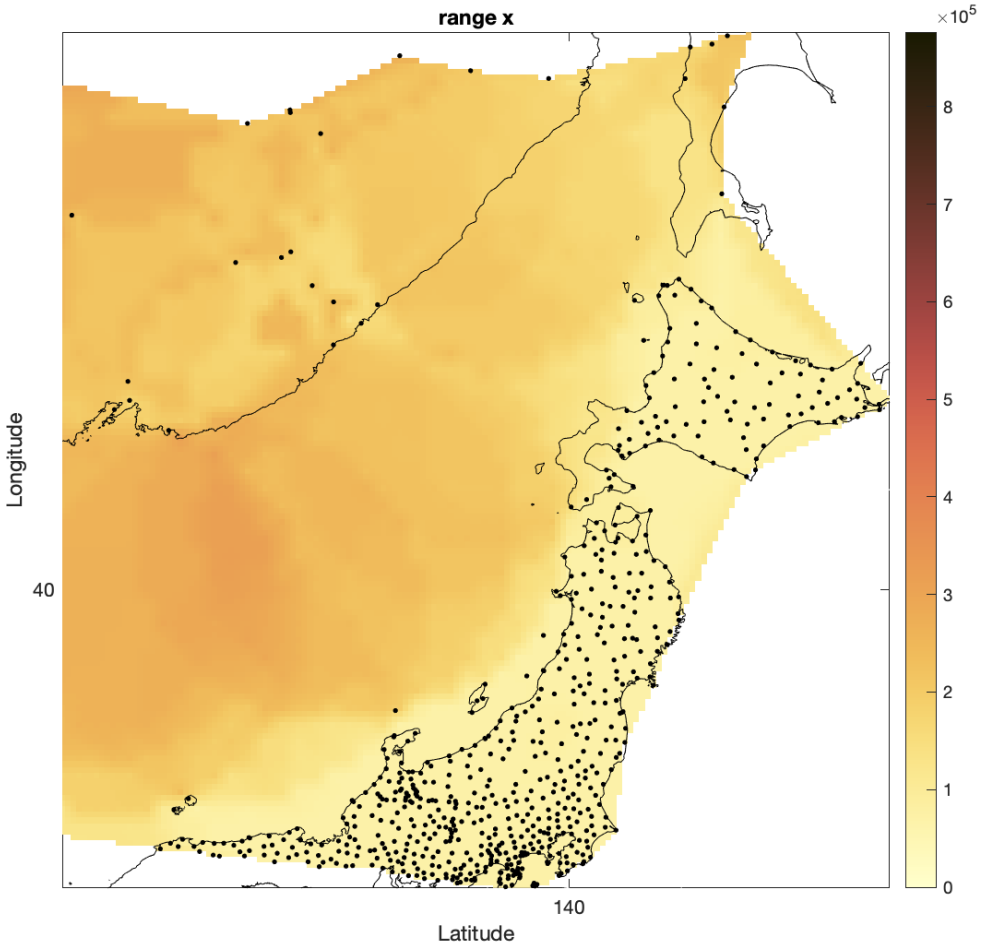
range x
×10^5
8
7
6
5
4
3
2
1
0
Longitude
40
140
Latitude

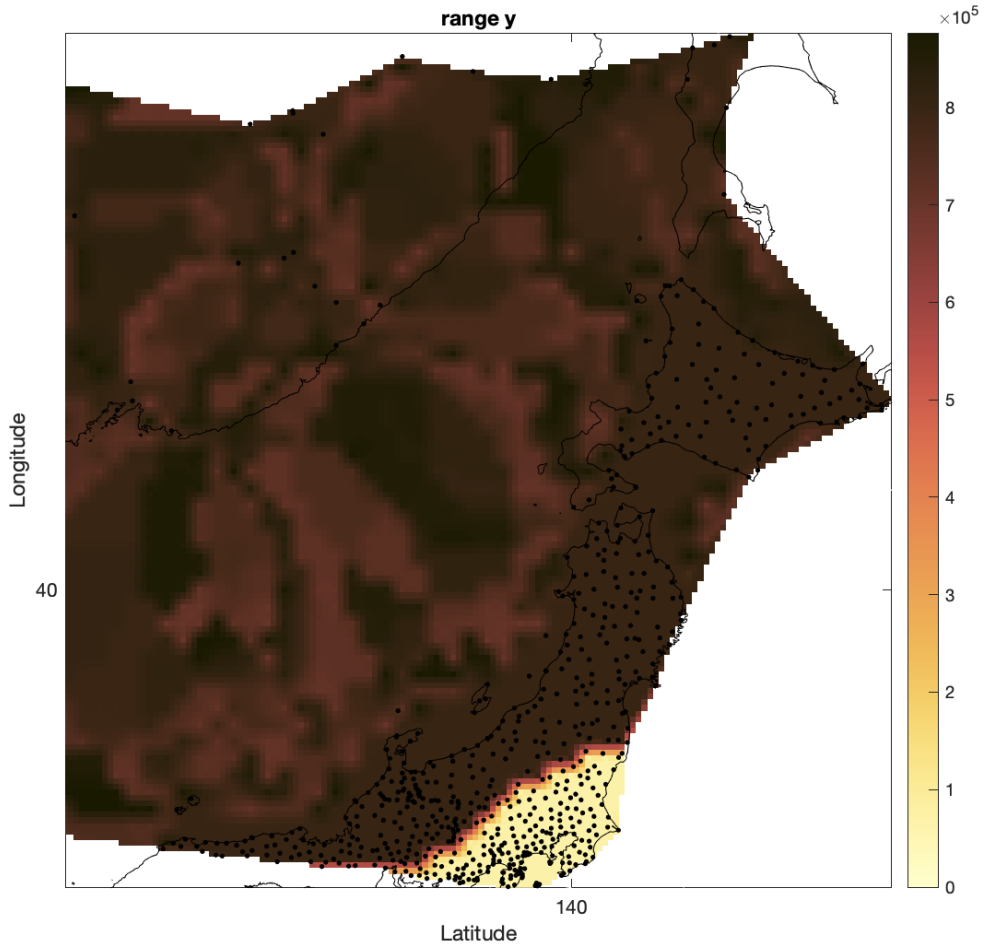

Figure S9 Estimated local correlogram (exponentional) parameters: range and variance, for trench-perpendicular (x) and trench-parallel (y) velocities in Japan. Range (in meters) describes the decay of the correlation with distance, variance denotes the local observation variance (in mm^2/yr^2). The variance is generally larger if the observation changes much within a natural neighborhood (roughly in between observation points) or in some cases, when the kernel radius is large because of a low signal-to-noise. The latter is the case for the trench-parallel variances, as the reported uncertainties are larger than the parallel signal. Still, we find a consistent parallel signal in most of the domain, which suggests that the error is overestimated.

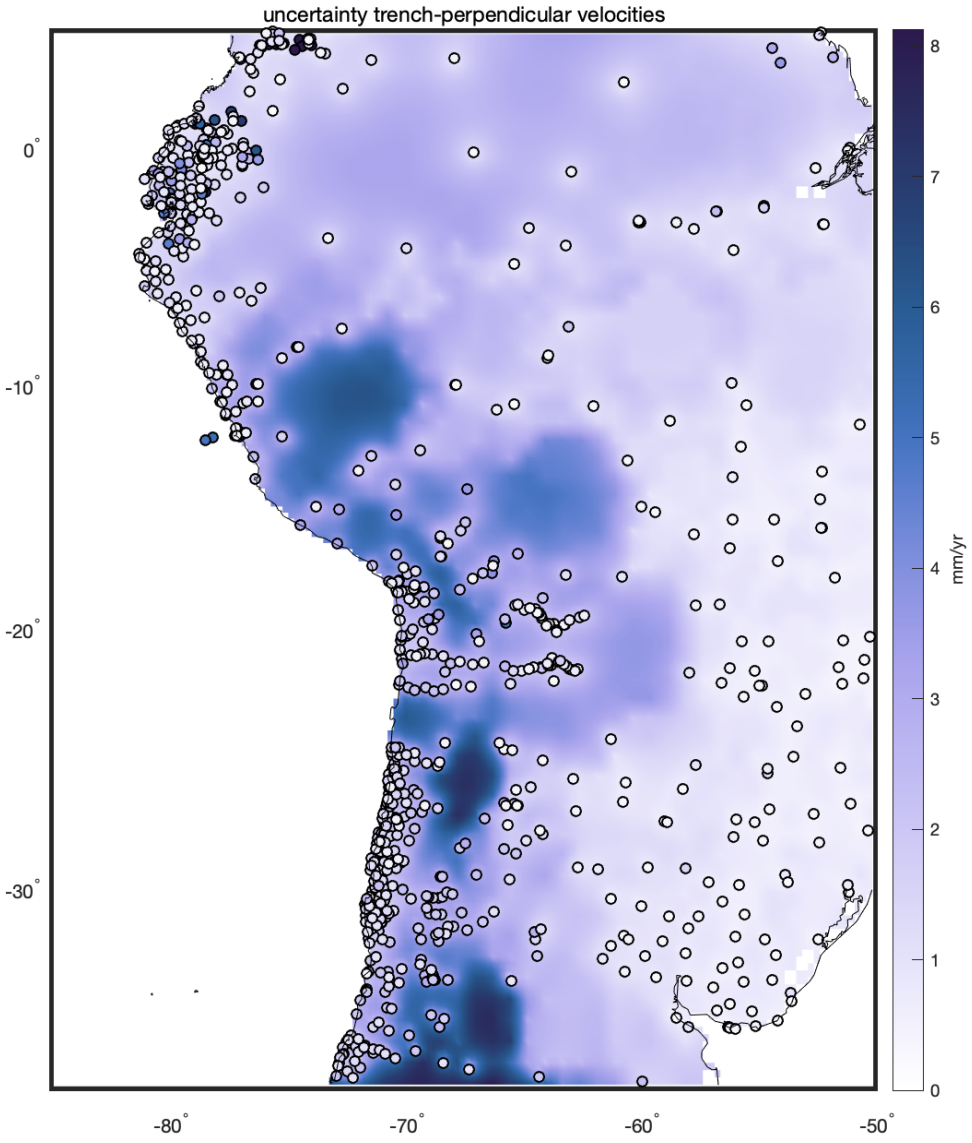
uncertainty trench-perpendicular velocities
0°
-10°
-20°
-30°
-80°
-70°
-60°
-50°
8
7
6
5
4
3
2
1
0
mm/yr

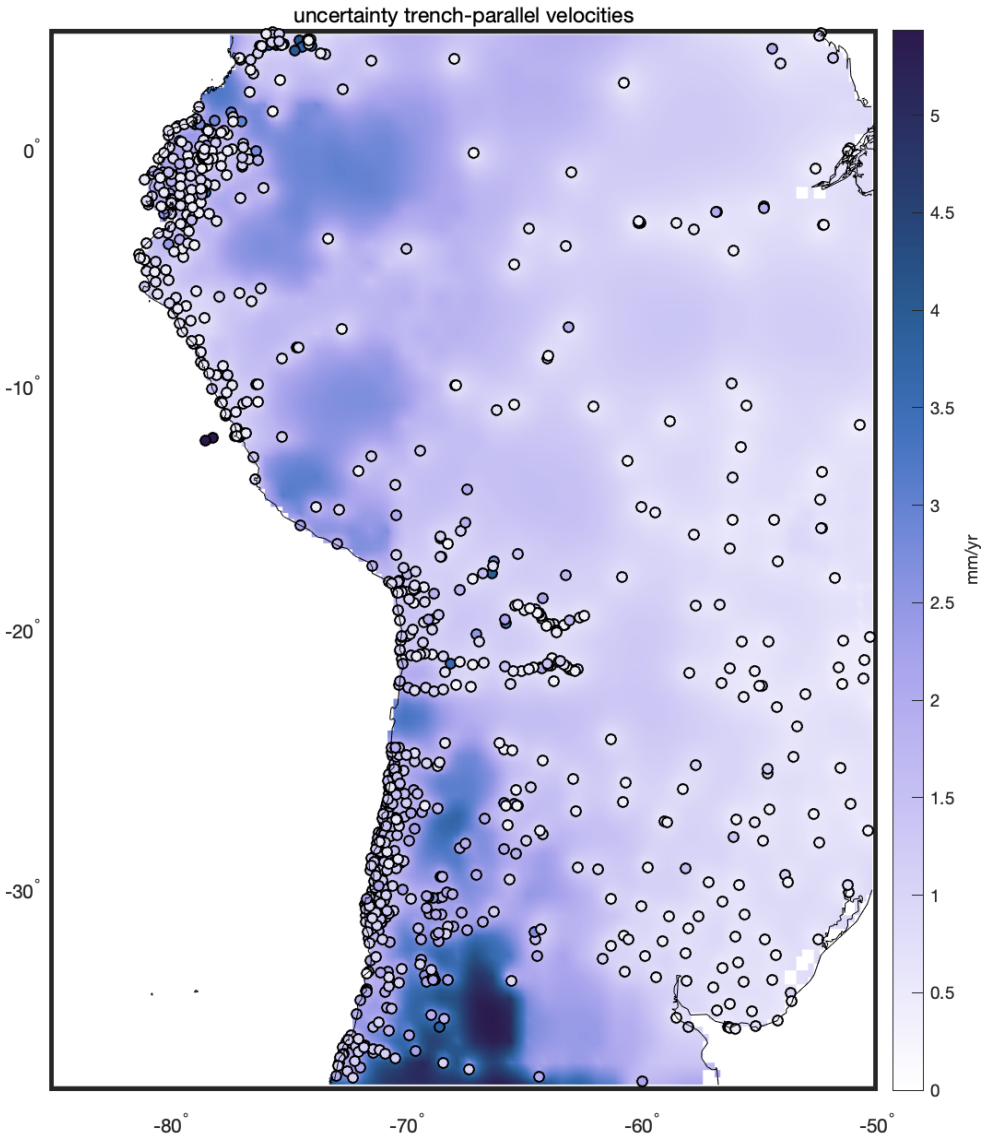

Figure S10 Uncertainy estimates (1 standard deviation) from the local ordinary kriging, trench-perpendicular and trench-parallel directions, for interseismic velocities in South America. In kriging uncertainties depend on both (local) variance, as well as on observation variance. In our implementation of local ordinary kriging uncertainties are large in areas with large gradients (especially when natural neighbors are relatively far apart), and small in areas with small gradients, see Figure 2 in the main text for the interpolated field. Circles denote the GNSS velocity uncertainties.

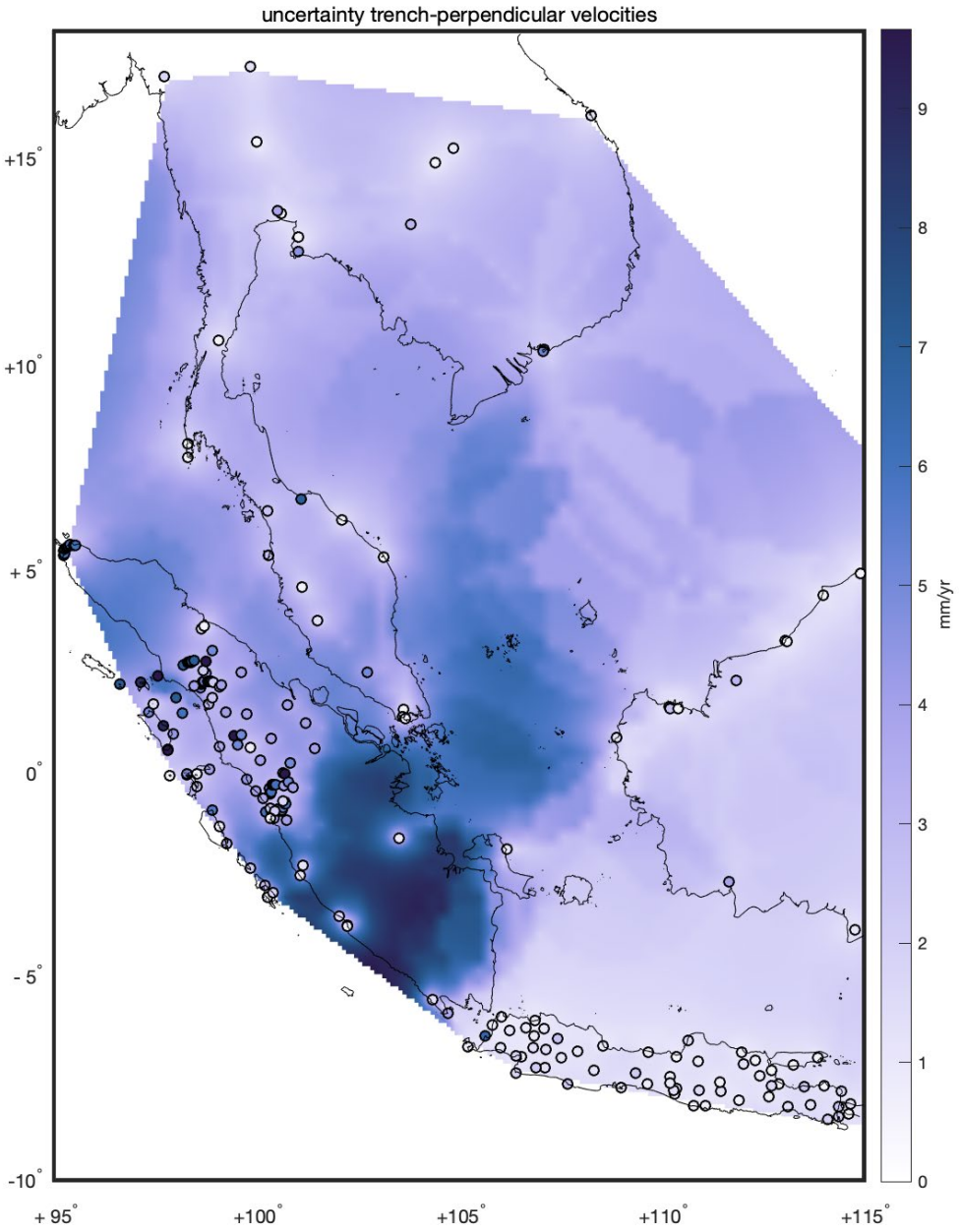
uncertainty trench-perpendicular velocities
+15°
+10°
+ 5°
0°
- 5°
-10°
+ 95°
+100°
+105°
+110°
+115°
9
8
7
6
5
4
3
2
1
0
mm/yr

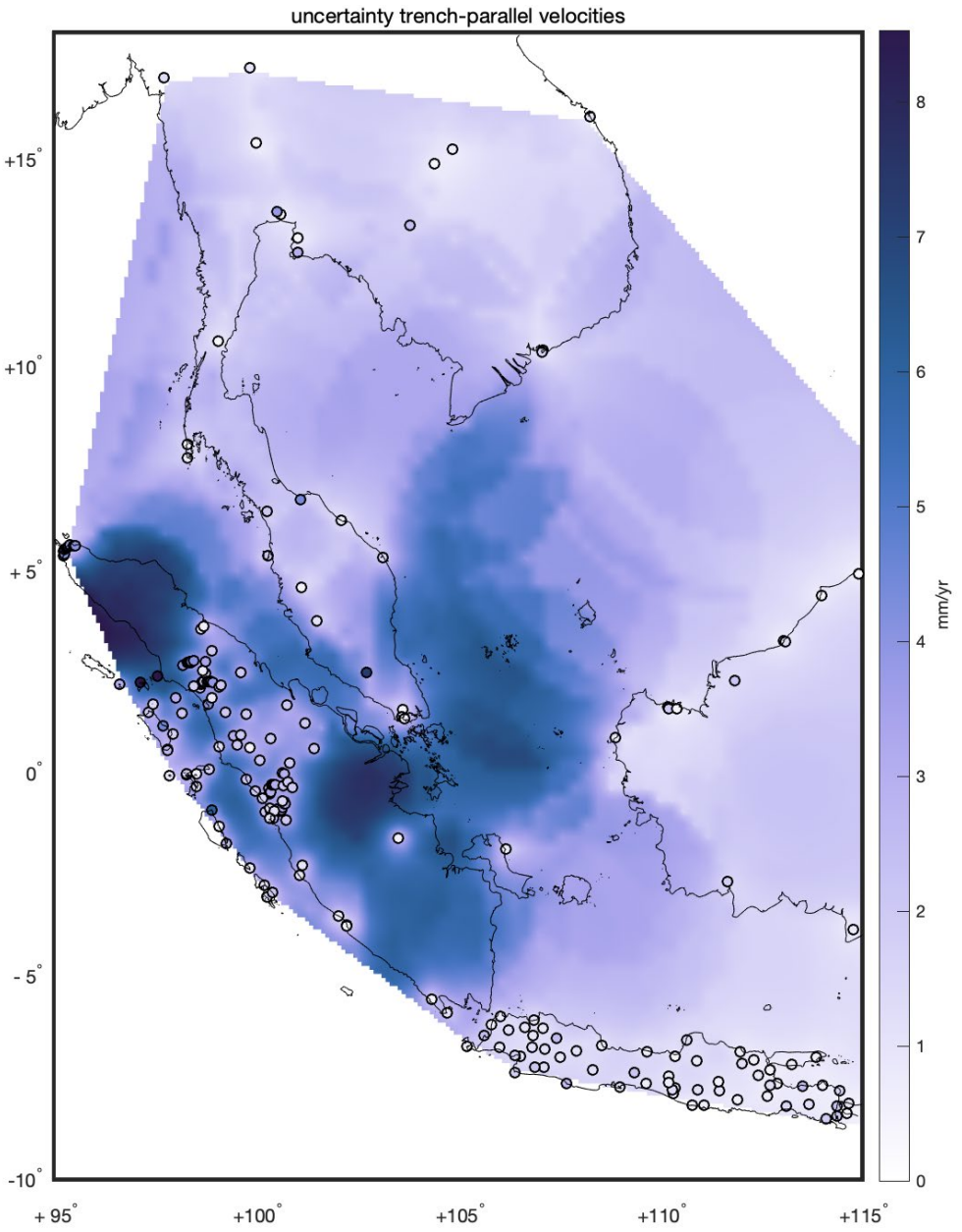

Figure S11 Uncertainy estimates (1 standard deviation) from the local ordinary kriging, trench-perpendicular and trench-parallel directions, for interseismic velocities in Southeast Asia. In kriging uncertainties depend on both (local) variance, as well as on observation variance. In our implementation of local ordinary kriging uncertainties are large in areas with large gradients (especially when natural neighbors are relatively far apart), and small in areas with small gradients, see Figure 2 in the main text for the interpolated field. Circles denote the GNSS velocity uncertainties.

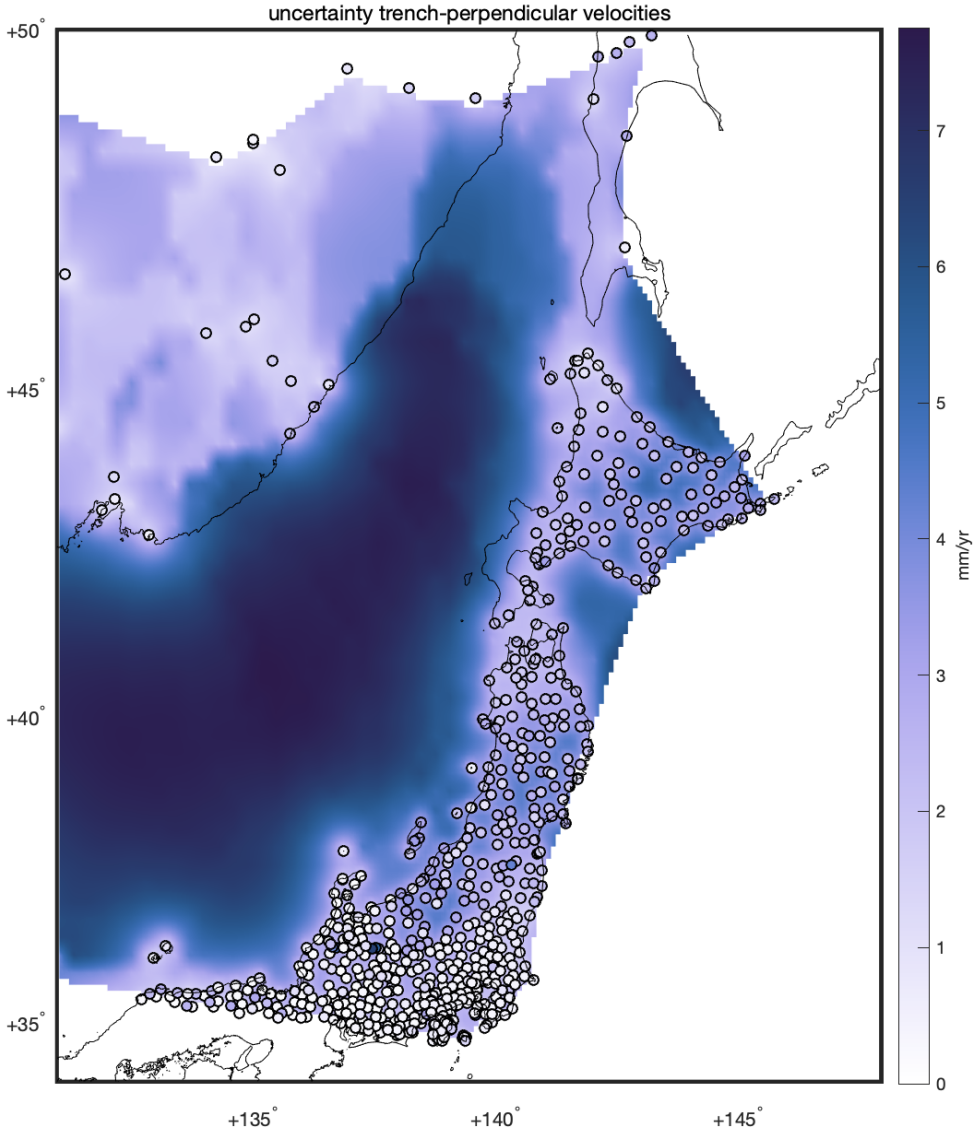
uncertainty trench-perpendicular velocities
+50°
+45°
+40°
+35°
+135°
+140°
+145°
7
6
5
4
3
2
1
0
mm/yr

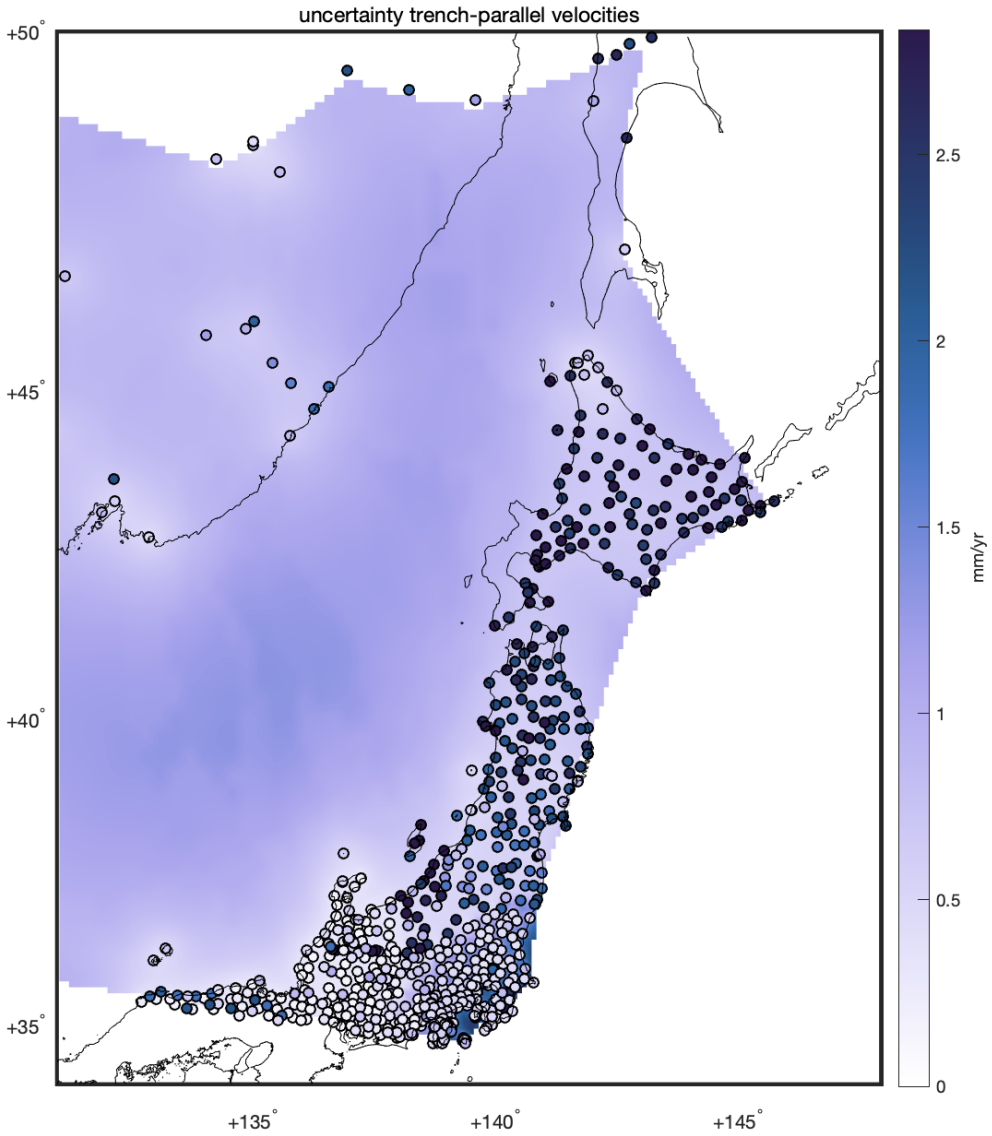

Figure S12. Uncertainy estimates (1 standard deviation) from the local ordinary kriging, trench-perpendicular and trench-parallel directions, for interseismic velocities in Japan. In kriging uncertainties depend on both (local) variance, as well as on observation variance. In our implementation of local ordinary kriging uncertainties are large in areas with large gradients (especially when natural neighbors are relatively far apart), and small in areas with small gradients, see Figure 2 in the main text for the interpolated field. Circles denote the GNSS velocity uncertainties.

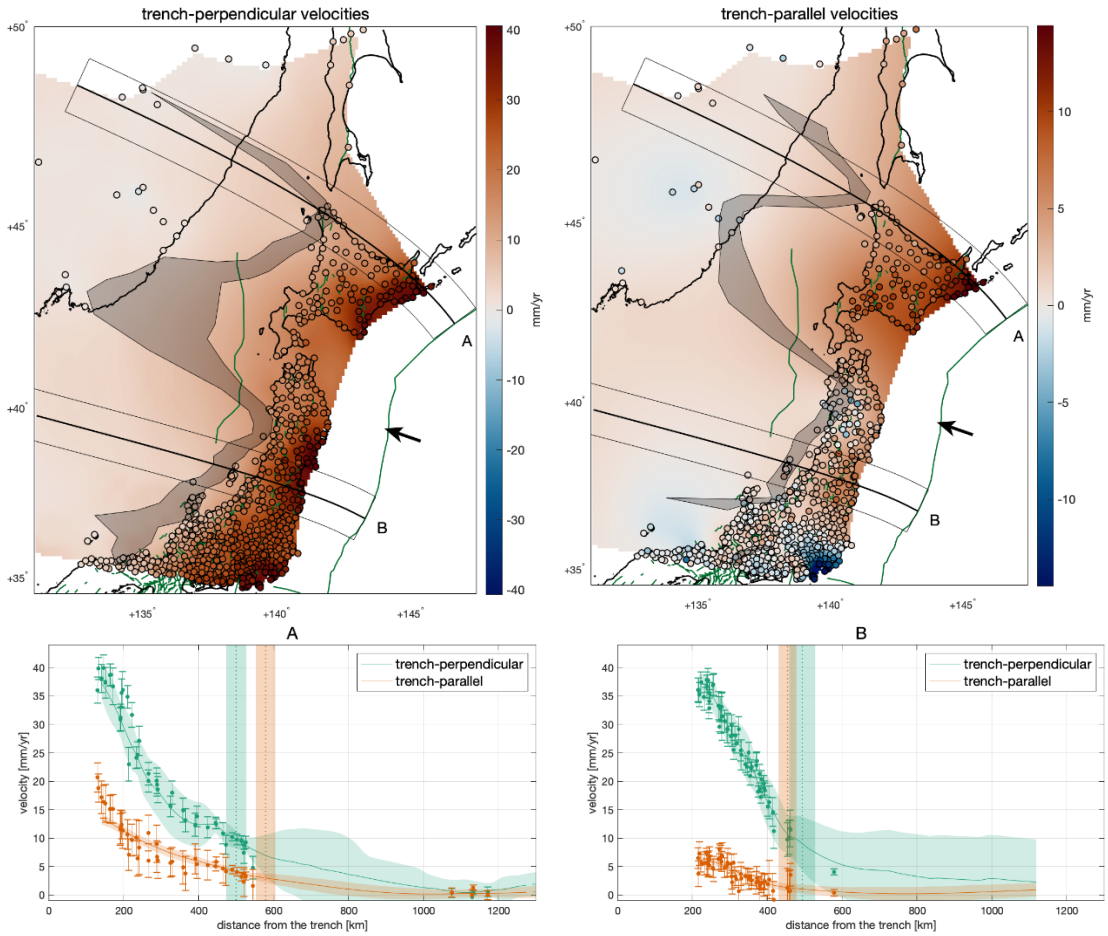

Figure S13. Results of the analysis of velocities in Japan, expressed in an Amur plate reference frame, rather than an Okhotsk plate reference frame as in Figure 4. The maps show interpolated trench-perpendicular (positive landward) and trench-parallel (positive left-lateral) velocity fields with 95% confidence-interval location of the hurdle, together with active faults in green from GEM (Styron & Pagani, 2020). Coastlines are in black and arrows show the interplate convergence direction between the Pacific plate and the Amur plate (Kreemer et al., 2014). Below, we show selected trench-perpendicular profiles, in Honshu and Hokkaido, on the landward side of the Japan Trench, along the profile lines traced in the maps. The velocity profiles show both interpolated velocity components with 1 standard deviation uncertainty (transparent bands), and the velocity components at GNSS stations within the swath with 1 standard deviation error bars. Note that the interpolated velocities are based on all GNSS velocity estimates, and not only those shown in the swath for reference. Vertical green and orange lines and bands outline estimated hurdle distances with 95% confidence intervals.

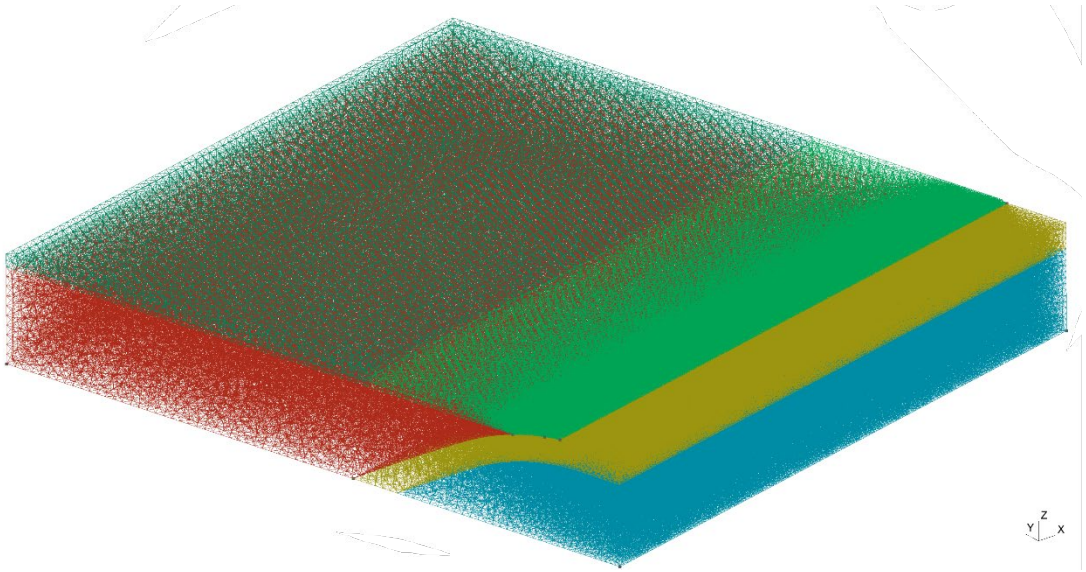

Figure S14. Isometric projection of the finite element mesh used in our numerical models.

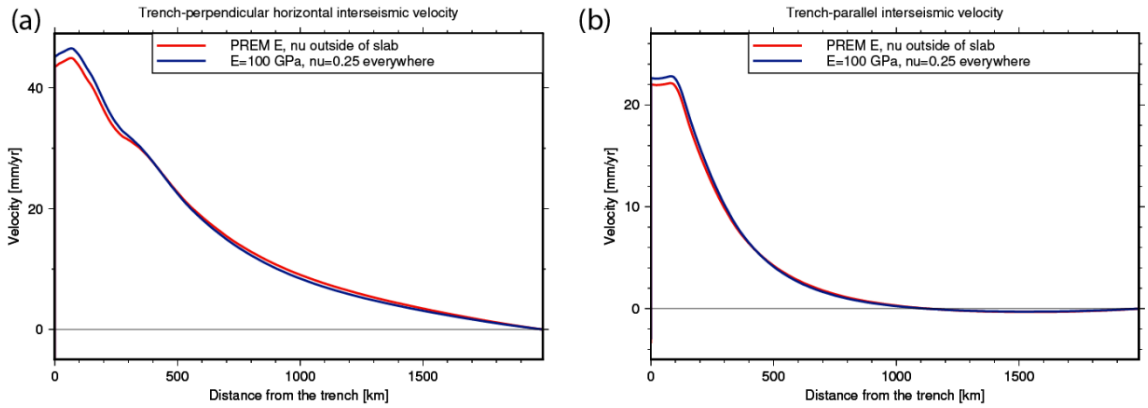

Figure S15. Trench-perpendicular profiles at *y*=0 through the interseismic horizontal surface velocity components, trench-perpendicular (a) and trench-parallel (b), respectively, for a model with elastic moduli according to the vertical profile of PREM (Dziewonski and Anderson, 1981) or constant, uniform values. In the slab, E is 100 GPa and ν is 0.25 in both models.

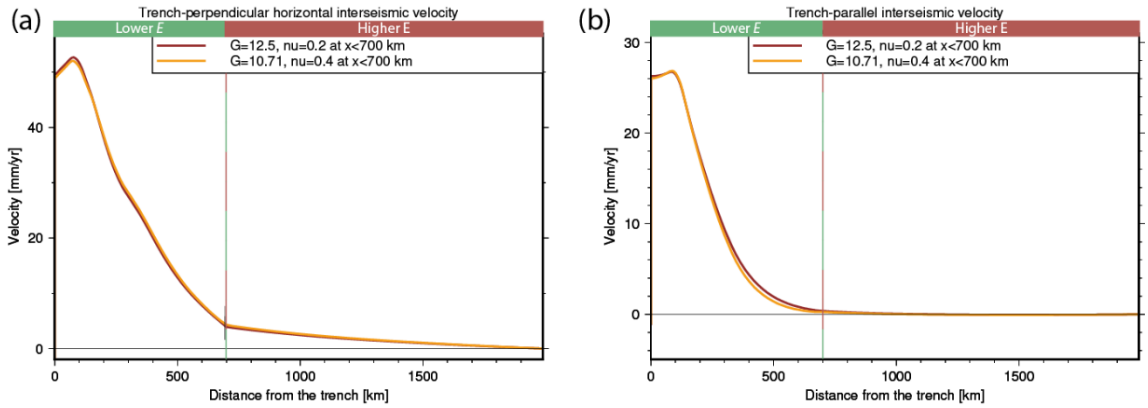

Figure S16. Trench-perpendicular profiles at y=0 through the interseismic horizontal surface velocity components, trench-perpendicular (a) and trench-parallel (b), respectively, for models with the same contrast in overriding plate E (30 GPa at x<700 km, 150 GPa at x>700 km), the same overriding plate G (87.5 GPa) and v (0.2) at x>700 km, and an overriding plate G at x<700 km of either 12.5 GPa (same v=0.2 as at x>700 km, same 1:7 ratio to far-field G as between near-field and far-field E) or 10.71 GPa (v=0.2 1:8.17 ratio to far-field G).

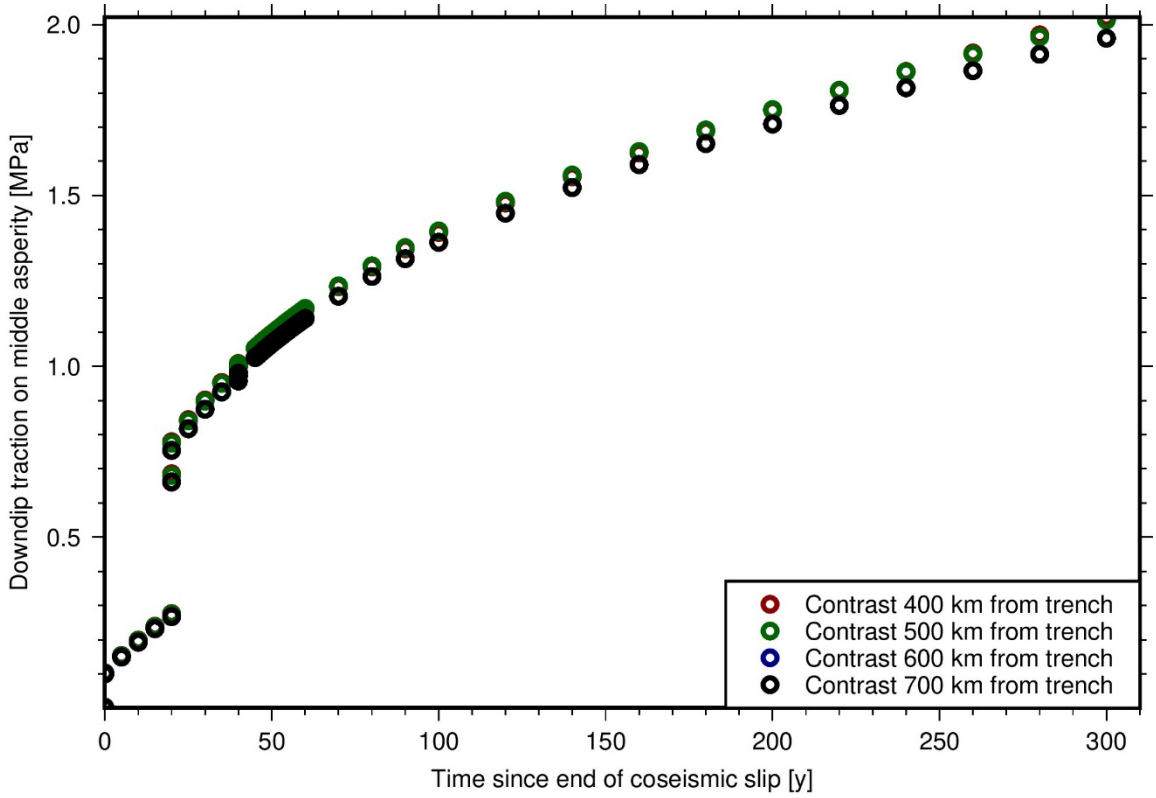

Figure S17. Plot of average traction in the downdip direction (interface-parallel, along parallel lines on the interface intersecting the trench at right angles) on the central asperity on the megathrust interface, through time over an earthquake cycle, in models with different horizontal distance between the trench and the contrast in E (10 GPa near-trench, 100 GPa elsewhere). The earthquake on the middle asperity happens at time 0, while the earthquakes on the intermediate and external asperities happen at time 20 and 40 years, respectively.

Study	Observational Period	Reference frame	Region of interest
Kendrick et al. (2001)	1993-2001	IGS08[a]	23°S-10°S
Klotz et al. (2001)	1994-1996	IGS08[a]	22°S-42°S

Brooks et al. (2003)	1993-2001	IGS08[a]	26°S-36°S
Chlieh et al. (2004)	1996-2000	IGS08[a]	23°S-18°S
Gagnon et al. (2005)	2001-2004	IGS08[a]	14°S-11°S
Ruegg et al. (2009)	1996-2002	IGS08[a]	37°S-35°S
Seemüller et al. (2010)	2000-2010	ITRF2008	South America
Brooks et al. (2011)	2000-2003	IGS08[a]	22°S-19°S
Cisneros and Nocquet (2011)	1995-2012	IGS08[a]	5°S-2°N
Drewes and Heidbach (2012)	1995-2009	IGS08[a]	South America
Métois et al. (2012)	1993-2009	ITRF2005[b]	38°S-24°S
Métois et al. (2013)	2000-2012	IGS08[a]	24°S-18°S
Métois et al. (2014)	2004-2012	ITRF2008	30°S-24°S
Nocquet et al. (2014)	1994-2012	ITRF2008[c]	12°S-2°N
Alvarado et al. (2014)	1996-2012	IGS08[a]	1°S-1°N
Villegas-Lanza et al. (2016)	2007-2013	ITRF2008[d]	18°S-2°S
Weiss et al. (2016)	2000-2007	Stable plate[e,f]	24°S-16°S
McFarland et al. (2017)	2010-2014	ITRF2008[g]	29°S-21°S
Klein et al. (2018)	2010-2015	ITRF2008	30°S-22°S
Blewitt et al. (2016)	1996-2021	IGS14[h]	global

Table S1. Overview of the collection of horizontal velocities for the South American margin, including the source, the observational period, the reference frame in which the velocities are reported. [a]We make use of the velocities expressed by Kreemer et al. 2014), where all previously published velocities have been transformed to IGS08 in a global inversion to estimate rotation and translation rates based on common sites. [b] We apply the rotation pole 25.4S, 124.6W, 0.11°/Myr as provided in Metois et al. (2012) to transform back to ITRF2005. [c] We apply the rotation pole 18.83S, 132.21W, 0.121°/Myr as provided by the authors to transform the published plate referenced velocities back to ITRF2008. [d] We apply the rotation pole 18.66S, 132.72W, 0.118°/Myr as provided in the supplementary information of Villegas-Lanza et al. (2016) to transform back to ITRF2008. [e] Weiss et al. (2016) use a South America plate reference, constructed with 44 cGPS sites, mostly located in Brazil, without a prior global solution. [f] Weiss et al. (2016) apply a postseimic correction

of the 2007 Tocapilla M_w 7.7 earthquake to the velocity estimates, by removing an empirically estimated coseismic step and postseismic decay function. [g] McFarland et al. (2017) used the ITRF2008 South American plate motion model (Altamimi et al., 2012), which we subsequently use to transform back to ITRF2008. [h] We exclude sites SURY RAS PRMA LSJ1 SPBP NXRA LDO LPLN, for which anomalously high velocities have been determine, in comparison to neighboring sites.

Study	Observational Period	Reference frame	Region of interest
Genrich et al. (2000)	1989-1996	IGS08[a]	Sumatra Fault
Bock et al. (2003)	1991-2001	IGS08[a]	Sunda plate
Simons et al. (2007)	1994-2004	IGS08[a]	Sunda plate
Chlieh et al. (2008)	2002-2004	IGS08[a]	Sumatra trench
Prawirodirdjo et al. (2010)	1991-2001[b] 2001-2007[c] 2002-2006[d]	IGS08[a]	Sumatra trench
Kreemer et al. (2014)	1990-2014[e]	IGS08	global
Koulali et al. (2017)	2002-2014[f]	ITRF2008[g]	Java

Table S2. Overview of the collection of horizontal velocities for the Sunda margin, including the source, the observational period, the reference frame in which the velocities are reported [a] We make use of the velocities expressed by Kreemer et al. (2014), where all previously published velocities have been transformed to IGS08 in a global inversion to estimate rotation and translation rates based on common sites.[b] Sites from the 1991-2001 have not been affected by major earthquakes, [c,d] and we do not use the data from the 2001-2007 and 2002-2006 tables in areas affected by the 2004 Sumatra-Andaman earthquake and the 2005 Nias earthquakes. [e] We use the table with exclusion periods for individual sites to be able to filter sites that are potentially affected by postseismic transients. [f] Velocities obtained from data after the 2006 M_w 7.7 earthquake in west Java has been corrected for coseismic offsets and postseismic transients using a best-fit viscoelastic model. [g] Published velocities in Koulali et al. (2017) are expressed in a Sunda plate reference, we

use the Euler pole that we received from the authors to express velocities in ITRF2008. Euler pole parameters: longitude 81.07°W, latitude 32.66°N, angular velocity 0.435924°/Myr.

Study	Observational period	Reference Frame	Region of interest
Sagiya et al., (2000)	1995-2000	IGS08[a]	Japan
Apel et al., (2006)	1995-2006	IGS08[a]	northeast Asia
Jin and Park, (2006)	2000-2003	IGS08[a]	South Korea
Hashimoto et al. (2009)	1996-2000	IGS08[a,b]	Japan
(Liu et al., 2010)	1996-2005	IGS08[a]	southwest Japan
(Shestakov et al., 2011)	1997-2009	IGS08[a]	northeast Asia
(Nishimura, 2011)	2007-2009	IGS08[a]	southwest Japan
(Ohzono et al., 2011)	1998-2006	IGS08[a]	central Japan
(Yoshioka, 2013)	2005-2009	IGS08[a]	southwest Japan
Shen (2013), contained in Kreemer et al. (2014)	1990-2013	IGS08[a]	northeast Asia
(Kreemer et al., 2014)	1990-2014[c]	IGS08[a]	global

Table S3 Overview of the collection of horizontal velocities for the Japan margin in the pre-2011 Tohoku earthquake period, including the source, the observational period, the reference frame in which the velocities are reported. [a] We make use of the velocities expressed by Kreemer et al. (2014), where all previously published velocities have been transformed to IGS08 in a global inversion to estimate rotation and translation rates based on common sites. b (Hashimoto et al., 2009) have corrected for transients of the 1994 Sanriku earthquake. [c] We exclude sites that have velocity estimates based partly on post-2011 Tohoku data.

References

Altamimi, Z., Métivier, L., Collilieux, X., 2012. ITRF2008 plate motion model: ITRF2008 PLATE MOTION MODEL. J. Geophys. Res. 117, n/a-n/a. https://doi.org/10.1029/2011JB008930

Alvarado, A., Audin, L., Nocquet, J.M., Lagreulet, S., Segovia, M., Font, Y., Lamarque, G., Yepes, H., Mothes, P., Rolandone, F., Jarrín, P., Quidelleur, X., 2014. Active

tectonics in Quito, Ecuador, assessed by geomorphological studies, GPS data, and crustal seismicity. Tectonics 33, 67–83. https://doi.org/10.1002/2012TC003224

Apel, E.V., Bürgmann, R., Steblov, G., Vasilenko, N., King, R., Prytkov, A., 2006. Independent active microplate tectonics of northeast Asia from GPS velocities and block modeling. Geophys. Res. Lett. 33, 2006GL026077. https://doi.org/10.1029/2006GL026077

Blewitt, G., Kreemer, C., Hammond, W.C., Gazeaux, J., 2016. MIDAS robust trend estimator for accurate GPS station velocities without step detection. Journal of Geophysical Research: Solid Earth 121, 2054–2068. https://doi.org/10.1002/2015JB012552

Bock, Y., Prawirodirdjo, L., Genrich, J.F., Stevens, C.W., McCaffrey, R., Subarya, C., Puntodewo, S.S.O., Calais, E., 2003. Crustal motion in Indonesia from Global Positioning System measurements. Journal of Geophysical Research: Solid Earth 108. https://doi.org/10.1029/2001JB000324

Brooks, B.A., Bevis, M., Smalley, R., Kendrick, E., Manceda, R., Lauría, E., Maturana, R., Araujo, M., 2003. Crustal motion in the Southern Andes (26°–36°S): Do the Andes behave like a microplate? Geochemistry, Geophysics, Geosystems 4. https://doi.org/10.1029/2003GC000505

Brooks, B.A., Bevis, M., Whipple, K., Ramon Arrowsmith, J., Foster, J., Zapata, T., Kendrick, E., Minaya, E., Echalar, A., Blanco, M., Euillades, P., Sandoval, M., Smalley, R.J., 2011. Orogenic-wedge deformation and potential for great earthquakes in the central Andean backarc. Nature Geoscience 4, 380–383. https://doi.org/10.1038/ngeo1143

Chlieh, M., Avouac, J.P., Sieh, K., Natawidjaja, D.H., Galetzka, J., 2008. Heterogeneous coupling of the Sumatran megathrust constrained by geodetic and paleogeodetic measurements. Journal of Geophysical Research: Solid Earth 113. https://doi.org/10.1029/2007JB004981

Chlieh, M., De Chabalier, J.B., Ruegg, J.C., Armijo, R., Dmowska, R., Campos, J., Feigl, K.L., 2004. Crustal deformation and fault slip during the seismic cycle in the North Chile subduction zone, from GPS and InSAR observations. Geophysical Journal International 158, 695–711. https://doi.org/10.1111/j.1365-246X.2004.02326.x

Cisneros, D., Nocquet, J., 2011. Campo de velocidades del Ecuador, obtenido a través de mediciones de campañes GPS de los ultimos 15 años y medidas de une red GPS permanente.

Conn, A.R., Gould, N.I.M., Toint, P.L., 2000. Trust Region Methods. SIAM.

Drewes, H., Heidbach, O., 2012. The 2009 Horizontal Velocity Field for South America and the Caribbean, in: Kenyon, S., Pacino, M.C., Marti, U. (Eds.), Geodesy for Planet Earth, International Association of Geodesy Symposia. Springer Berlin Heidelberg, Berlin, Heidelberg, pp. 657–664. https://doi.org/10.1007/978-3-642-20338-1_81

Dziewonski, A.M., Anderson, D.L., 1981. Preliminary reference Earth model. Physics of the Earth and Planetary Interiors 25, 297–356. https://doi.org/10.1016/0031-9201(81)90046-7

Fouedjio, F., Séguret, S., 2016. Predictive Geological Mapping Using Closed-Form Non-stationary Covariance Functions with Locally Varying Anisotropy: Case Study at El Teniente Mine (Chile). Nat Resour Res 25, 431–443. https://doi.org/10.1007/s11053-016-9293-4

Gagnon, K., Chadwell, C.D., Norabuena, E., 2005. Measuring the onset of locking in the Peru–Chile trench with GPS and acoustic measurements. Nature 434, 205–208. https://doi.org/10.1038/nature03412

Genrich, J.F., Bock, Y., McCaffrey, R., Prawirodirdjo, L., Stevens, C.W., Puntodewo, S.S.O., Subarya, C., Wdowinski, S., 2000. Distribution of slip at the northern Sumatran fault system. J. Geophys. Res. 105, 28327–28341. https://doi.org/10.1029/2000JB900158

Govers, R., Furlong, K.P., van de Wiel, L., Herman, M.W., Broerse, T., 2018. The Geodetic Signature of the Earthquake Cycle at Subduction Zones: Model Constraints on the Deep Processes. Reviews of Geophysics 56, 6–49. https://doi.org/10.1002/2017RG000586

Govers, R., Wortel, M.J.R., 2005. Lithosphere tearing at STEP faults: response to edges of subduction zones. Earth and Planetary Science Letters 236, 505–523. https://doi.org/10.1016/j.epsl.2005.03.022

Govers, R., Wortel, M.J.R., 1993. Initiation of asymmetric extension in continental lithosphere. Tectonophysics 223, 75–96. https://doi.org/10.1016/0040-1951(93)90159-H

Hashimoto, C., Noda, A., Sagiya, T., Matsu'ura, M., 2009. Interplate seismogenic zones along the Kuril–Japan trench inferred from GPS data inversion. Nature Geosci 2, 141–144. https://doi.org/10.1038/ngeo421

Jin, S., Park, P.-H., 2006. Strain accumulation in South Korea inferred from GPS measurements. Earth Planet Sp 58, 529–534. https://doi.org/10.1186/BF03351950

Kendrick, E., Bevis, M., Smalley, R., Brooks, B., 2001. An integrated crustal velocity field for the central Andes. Geochemistry, Geophysics, Geosystems 2. https://doi.org/10.1029/2001GC000191

Klein, E., Métois, M., Meneses, G., Vigny, C., Delorme, A., 2018. Bridging the gap between North and Central Chile: insight from new GPS data on coupling complexities and the Andean sliver motion. Geophysical Journal International 213, 1924–1933. https://doi.org/10.1093/gji/ggy094

Klotz, J., Khazaradze, G., Angermann, D., Reigber, C., Perdomo, R., Cifuentes, O., 2001. Earthquake cycle dominates contemporary crustal deformation in Central and Southern Andes. Earth and Planetary Science Letters 193, 437–446. https://doi.org/10.1016/S0012-821X(01)00532-5

Koulali, A., McClusky, S., Susilo, S., Leonard, Y., Cummins, P., Tregoning, P., Meilano, I., Efendi, J., Wijanarto, A.B., 2017. The kinematics of crustal deformation in Java from GPS observations: Implications for fault slip partitioning. Earth and Planetary Science Letters 458, 69–79. https://doi.org/10.1016/j.epsl.2016.10.039

Kreemer, C., Blewitt, G., Klein, E.C., 2014. A geodetic plate motion and Global Strain Rate Model. Geochemistry, Geophysics, Geosystems 15, 3849–3889. https://doi.org/10.1002/2014GC005407

Liu, Z., Owen, S., Dong, D., Lundgren, P., Webb, F., Hetland, E., Simons, M., 2010. Estimation of interplate coupling in the Nankai trough, Japan using GPS data from 1996 to 2006. GJI 181, 1313–1328. https://doi.org/10.1111/j.1365-246X.2010.04600.x

Machuca-Mory, D.F., Deutsch, C.V., 2013. Non-stationary Geostatistical Modeling Based on Distance Weighted Statistics and Distributions. Math Geosci 45, 31–48. https://doi.org/10.1007/s11004-012-9428-z

McFarland, P.K., Bennett, R.A., Alvarado, P., DeCelles, P.G., 2017. Rapid Geodetic Shortening Across the Eastern Cordillera of NW Argentina Observed by the Puna-Andes GPS Array. Journal of Geophysical Research 24. https://doi.org/10.1002/2017JB014739

Métois, M., Socquet, A., Vigny, C., 2012. Interseismic coupling, segmentation and mechanical behavior of the central Chile subduction zone. Journal of Geophysical Research: Solid Earth 117. https://doi.org/10.1029/2011JB008736

Métois, M., Socquet, A., Vigny, C., Carrizo, D., Peyrat, S., Delorme, A., Maureira, E., Valderas-Bermejo, M.-C., Ortega, I., 2013. Revisiting the North Chile seismic gap segmentation using GPS-derived interseismic coupling. Geophysical Journal International 194, 1283–1294. https://doi.org/10.1093/gji/ggt183

Métois, M., Vigny, C., Socquet, A., Delorme, A., Morvan, S., Ortega, I., Valderas-Bermejo, C.-M., 2014. GPS-derived interseismic coupling on the subduction and seismic hazards in the Atacama region, Chile. Geophysical Journal International 196, 644–655. https://doi.org/10.1093/gji/ggt418

Nishimura, T., 2011. Back-arc spreading of the northern Izu–Ogasawara (Bonin) Islands arc clarified by GPS data. Tectonophysics 512, 60–67. https://doi.org/10.1016/j.tecto.2011.09.022

Nocquet, J.-M., Villegas-Lanza, J.C., Chlieh, M., Mothes, P.A., Rolandone, F., Jarrin, P., Cisneros, D., Alvarado, A., Audin, L., Bondoux, F., Martin, X., Font, Y., Régnier, M., Vallée, M., Tran, T., Beauval, C., Maguiña Mendoza, J.M., Martinez, W., Tavera, H., Yepes, H., 2014. Motion of continental slivers and creeping subduction in the northern Andes. Nature Geosci 7, 287–291. https://doi.org/10.1038/ngeo2099

Ohzono, M., Sagiya, T., Hirahara, K., Hashimoto, M., Takeuchi, A., Hoso, Y., Wada, Y., Onoue, K., Ohya, F., Doke, R., 2011. Strain accumulation process around the Atotsugawa fault system in the Niigata-Kobe Tectonic Zone, central Japan: Strain

field around the Atotsugawa fault system. Geophysical Journal International 184, 977–990. https://doi.org/10.1111/j.1365-246X.2010.04876.x

Prawirodirdjo, L., McCaffrey, R., Chadwell, C.D., Bock, Y., Subarya, C., 2010. Geodetic observations of an earthquake cycle at the Sumatra subduction zone: Role of interseismic strain segmentation. Journal of Geophysical Research: Solid Earth 115. https://doi.org/10.1029/2008JB006139

Ruegg, J.C., Rudloff, A., Vigny, C., Madariaga, R., de Chabalier, J.B., Campos, J., Kausel, E., Barrientos, S., Dimitrov, D., 2009. Interseismic strain accumulation measured by GPS in the seismic gap between Constitución and Concepción in Chile. Physics of the Earth and Planetary Interiors, Earthquakes in subduction zones: A multidisciplinary approach 175, 78–85. https://doi.org/10.1016/j.pepi.2008.02.015

Sagiya, T., Miyazaki, S., Tada, T., 2000. Continuous GPS Array and Present-day Crustal Deformation of Japan. Pure appl. geophys. 2303–2322.

Seemüller, W., Sánchez, L., Seitz, M., Drewes, H., 2010. The position and velocity solution SIR10P01 of the IGS Regional Network Associate Analysis Centre for SIRGAS (IGS RNAAC SIR).

Shestakov, N.V., Gerasimenko, M.D., Takahashi, H., Kasahara, M., Bormotov, V.A., Bykov, V.G., Kolomiets, A.G., Gerasimov, G.N., Vasilenko, N.F., Prytkov, A.S., Timofeev, V.Yu., Ardyukov, D.G., Kato, T., 2011. Present tectonics of the southeast of Russia as seen from GPS observations: Present tectonics of the southeast of Russia. Geophysical Journal International 184, 529–540. https://doi.org/10.1111/j.1365-246X.2010.04871.x

Sibson, R., 1981. A brief description of natural neighbour interpolation. Interpreting Multivariate Data.

Simons, W.J.F., Socquet, A., Vigny, C., Ambrosius, B. a. C., Abu, S.H., Promthong, C., Subarya, C., Sarsito, D.A., Matheussen, S., Morgan, P., Spakman, W., 2007. A decade of GPS in Southeast Asia: Resolving Sundaland motion and boundaries. Journal of Geophysical Research: Solid Earth 112. https://doi.org/10.1029/2005JB003868

Villegas-Lanza, J.C., Chlieh, M., Cavalié, O., Tavera, H., Baby, P., Chire-Chira, J., Nocquet, J.-M., 2016. Active tectonics of Peru: Heterogeneous interseismic

coupling along the Nazca megathrust, rigid motion of the Peruvian Sliver, and Subandean shortening accommodation. Journal of Geophysical Research: Solid Earth 121, 7371–7394. https://doi.org/10.1002/2016JB013080

Wackernagel, H., 2003. Ordinary Kriging, in: Wackernagel, H. (Ed.), Multivariate Geostatistics: An Introduction with Applications. Springer, Berlin, Heidelberg, pp. 79–88. https://doi.org/10.1007/978-3-662-05294-5_11

Wang, K., Hu, Y., Bevis, M., Kendrick, E., Smalley, R., Vargas, R.B., Lauría, E., 2007. Crustal motion in the zone of the 1960 Chile earthquake: Detangling earthquake-cycle deformation and forearc-sliver translation: CHILE EARTHQUAKE CRUSTAL MOTION. Geochem. Geophys. Geosyst. 8. https://doi.org/10.1029/2007GC001721

Weiss, J.R., Brooks, B.A., Foster, J.H., Bevis, M., Echalar, A., Caccamise, D., Heck, J., Kendrick, E., Ahlgren, K., Raleigh, D., Smalley, R., Vergani, G., 2016. Isolating active orogenic wedge deformation in the southern Subandes of Bolivia. Journal of Geophysical Research: Solid Earth 121, 6192–6218. https://doi.org/10.1002/2016JB013145

Yoshioka, S., 2013. Interplate coupling along the Nankai Trough, southwest Japan, inferred from inversion analyses of GPS data: Effects of subducting plate geometry and spacing of hypothetical ocean-bottom GPS stations 10.